Monthly Notices
of the
ROYAL ASTRONOMICAL SOCIETY

MNRAS **472,** 1716–1735 (2017)
Advance Access publication 2017 August 14

doi:10.1093/mnras/stx2042

Magnetic activity and radial velocity filtering of young Suns: the weak-line T-Tauri stars Par 1379 and Par 2244

C. A. Hill,[1]★ A. Carmona,[1] J.-F. Donati,[1] G. A. J. Hussain,[1,2] S. G. Gregory,[3] S. H. P. Alencar,[4] J. Bouvier[5] and the MaTYSSE collaboration

[1]*IRAP, Université de Toulouse, CNRS, UPS, CNES, 14 Avenue Edouard Belin, Toulouse, F-31400, France*
[2]*ESO, Karl-Schwarzschild-Str. 2, D-85748 Garching, Germany*
[3]*SUPA, School of Physics and Astronomy, University of St Andrews, St Andrews, Scotland KY16 9SS, UK*
[4]*Departamento de Fisica – ICEx-UFMG, Av. Antônio Carlos, 6627, 30270–901 Belo Horizonte, MG, Brazil*
[5]*Université Grenoble Alpes, CNRS, IPAG, F-38000 Grenoble, France*

Accepted 2017 August 7. Received 2017 August 7; in original form 2017 March 20

ABSTRACT

We report the results of our spectropolarimetric monitoring of the weak-line T-Tauri stars (wTTSs) Par 1379 and Par 2244, within the MaTYSSE (Magnetic Topologies of Young Stars and the Survival of close-in giant Exoplanets) programme. Both stars are of a similar mass (1.6 and 1.8 $M_{\odot}$) and age (1.8 and 1.1 Myr), with Par 1379 hosting an evolved low-mass dusty circumstellar disc, and with Par 2244 showing evidence of a young debris disc. We detect profile distortions and Zeeman signatures in the unpolarized and circularly polarized lines for each star, and have modelled their rotational modulation using tomographic imaging, yielding brightness and magnetic maps. We find that Par 1379 harbours a weak (250 G), mostly poloidal field tilted 65° from the rotation axis. In contrast, Par 2244 hosts a stronger field (860 G) split 3:2 between poloidal and toroidal components, with most of the energy in higher order modes, and with the poloidal component tilted 45° from the rotation axis. Compared to the lower mass wTTSs, V819 Tau and V830 Tau, Par 2244 has a similar field strength, but is much more complex, whereas the much less complex field of Par 1379 is also much weaker than any other mapped wTTS. We find moderate surface differential rotation of 1.4× and 1.8× smaller than Solar, for Par 1379 and Par 2244, respectively. Using our tomographic maps to predict the activity-related radial velocity (RV) jitter, and filter it from the RV curves, we find RV residuals with dispersions of 0.017 and 0.086 km s^{-1} for Par 1379 and Par 2244, respectively. We find no evidence for close-in giant planets around either star, with 3σ upper limits of 0.56 and 3.54 M_{Jup} (at an orbital distance of 0.1 au).

Key words: techniques: polarimetric – stars: formation – stars: imaging – stars: individual: Par 1379 – stars: individual: Par 2244 – stars: magnetic field.

1 INTRODUCTION

Stellar magnetic fields have their largest impact during the early evolution of low-mass stars. T-Tauri stars (TTSs) are late-type pre-main-sequence (PMS) stars that are gravitationally contracting towards the MS, and are initially surrounded by a protoplanetary disc (e.g. André, Basu & Inutsuka 2009; Donati & Landstreet 2009). The radial contraction increases the density of the stellar interior, and eventually leads to the development of a radiative core (for stellar masses $\gtrsim$0.35 $M_{\odot}$, Chabrier & Baraffe 1997), where the core boundary is known as the tachocline. This change in stellar structure is thought to significantly alter the stellar dynamo mechanism, from one that is distributed throughout the convective zone, to a solar-like dynamo concentrated at the tachocline (e.g. Durney, De Young & Roxburgh 1993). Such changes to the underlying dynamo mechanism may exhibit themselves as variations in the resulting magnetic field topologies, and so observations of magnetic fields on young stars can lead to a better understanding of the behaviour and evolution of the underlying stellar dynamo mechanisms as the star evolves towards the zero-age main-sequence (ZAMS).

At an age of 0.5–10 Myr, TTS may be classified into two groups (based on their accretion status), known as classical T-Tauri stars (cTTSs) and weak-line T-Tauri stars (wTTSs). cTTSs are defined as

★ E-mail: chill@irap.omp.eu

TTS that are accreting material from a massive (presumably planet forming) disc, whereas wTTSs have exhausted the gas in their inner discs and are no longer accreting (or are accreting at a low level).

Magnetic fields of cTTSs play a vital role in controlling accretion process and triggering outflows, and largely dictate their angular momentum evolution (e.g. Bouvier et al. 2007; Frank et al. 2014). In particular, large-scale fields of cTTSs can evacuate the central regions of accretion discs, funnel the material on to the star, and enforce co-rotation between the star and the inner disc Keplerian flows, causing cTTSs to rotate more slowly than expected from the contraction and accretion of the disc material (e.g. Davies, Gregory & Greaves 2014). Furthermore, magnetic fields of cTTS and their discs can affect the formation and migration of planets (e.g. Baruteau et al. 2014). Moreover, fields of both cTTSs and wTTSs are known to trigger thermally driven winds through heating by accretion shocks and/or Alfvén waves (e.g. Cranmer 2009; Cranmer & Saar 2011), resulting in flares, coronal-mass ejections and angular momentum loss (e.g. Aarnio, Matt & Stassun 2012; Matt et al. 2012). It is clear then that characterizing magnetic fields in cTTSs and wTTSs is critical for testing and developing theoretical models (providing more physical realism), and trialling scenarios currently invoked to explain low-mass star and planet formation.

Magnetic fields were first detected on cTTSs nearly 20 yr ago (e.g. Johns-Krull, Valenti & Koresko 1999), and through the MaPP (Magnetic Protostars and Planets) Large Observing Programme allocated on ESPaDOnS on the 3.6-m Canada-France-Hawaii Telescope (CFHT), the large-scale topologies of 11 cTTSs have been revealed (e.g. Donati et al. 2007; Hussain et al. 2009; Donati et al. 2010a, 2013). Here, the large-scale stellar magnetic fields were mapped by performing an inversion of a time series of spectropolarimetric data, reconstructing the observed field with a spherical harmonic expansion, adopting a maximum-entropy approach. This technique (called Zeeman Doppler Imaging, ZDI) allows one to determine both the field strength and topology. This first survey revealed that the large-scale fields of cTTSs remain relatively simple and mainly poloidal when the host star is still fully or largely convective, but become much more complex when the host star turns mostly radiative (Gregory et al. 2012; Donati et al. 2013). This survey also showed that these fields are likely of dynamo origin, varying over time-scales of a few years (Donati et al. 2011, 2012, 2013), and resembling those of mature stars with comparable internal structure (Morin et al. 2008).

In the case of wTTSs, a total of five stars have been magnetically mapped to date (using ZDI), namely V410 Tau, LkCa 4, V819 Tau, V830 Tau and TAP 26 (Skelly et al. 2010; Carroll et al. 2012; Donati et al. 2014, 2015; Yu et al. 2017). These few stars show a much wider range of field topologies compared to cTTSs and MS dwarfs with similar internal structures, while V819 Tau and V830 Tau display a mostly poloidal field topology, V410 Tau and LkCa 4 show significant toroidal components despite being fully convective, in surprising contrast to fully convective cTTSs and mature M dwarfs that harbour relatively simple poloidal fields (Morin et al. 2008; Donati et al. 2013). This toroidal component may develop by the stellar dynamo being influenced by the rapid spin-up that TTS experience, due to their gravitational contraction and angular momentum conservation, once their discs have dispersed (see discussion in Donati et al. 2014).

Given that wTTSs are the transitional phase between cTTSs and ZAMS low-mass stars, studies of their magnetic topologies and associated winds are of great interest, as these are the initial conditions in which disc-less PMS stars initiate their unleashed spin-up as they contract towards the ZAMS. This is the goal of the MaTYSSE (Magnetic Topologies of Young Stars and the Survival of close-in giant Exoplanets) Large Programme, allocated at CFHT over semesters 2013a–2016b (510 h) with complementary observations with the NARVAL spectropolarimeter on the 2-m Telescope Bernard Lyot at Pic du Midi in France (420 h) and with the HARPS spectropolarimeter at the 3.6-m ESO Telescope at La Silla in Chile (70 h). As well as determining the magnetic topologies of ∼30 wTTSs and monitoring the long-term topology variability of ∼5 cTTSs, MaTYSSE will allow us to broadly study magnetic winds of wTTSs and corresponding spin-down rates (e.g. Vidotto et al. 2014). Furthermore, we are able to filter out most of the activity-related jitter from the radial velocity (RV) curves of wTTSs (using spectropolarimetry and doppler imaging to model surface activity) for potentially detecting hot Jupiters (hJs; see Donati et al. 2016), and thus verifying whether core accretion and migration is the most likely mechanism for forming close-in giant planets (e.g. Alibert et al. 2005).

Here, we present full analyses of the phase-resolved spectropolarimetric observations of Par 1379 and Par 2244, continuing our study of wTTSs in the framework of the MaTYSSE programme. For our study, we first document our observations in Section 2, then review the stellar and disc properties of both stars in Section 3. In Section 4, we describe the results obtained after applying our tomographic modelling technique to the data, and in Section 5, we use these results to filter out the activity jitter from the RV curves, and look for the potential presence of hJs around both stars. In Section 6, we discuss our results and their implications for understanding low-mass star and planet formation. Finally, in Section 7, we provide a summary of our results.

2 OBSERVATIONS

Spectropolarimetric observations of Par 1379 were taken in January 2014, with observations of Par 2244 taken in December 2014 and January 2015, both using ESPaDOnS at the 3.6-m CFHT. Spectra from ESPaDOnS span the entire optical domain (from 370 to 1000 nm) at a resolution of 65 000 (i.e. a resolved velocity element of 4.6 km s^{-1}) over the full wavelength range, in both circular or linear polarization (Donati 2003).

A total of 10 circularly polarized (Stokes *V*) and unpolarized (Stokes *I*) spectra were collected for Par 1379 over a time span of 14 nights, corresponding to around 2.3 rotation cycles. Time sampling was regular apart from a five night gap due to bad weather near the middle of the run. For Par 2244, 14 spectra were collected over a 25 night time span, corresponding to around 9.2 rotation cycles. Time sampling for these spectra was irregular, with a six night gap after the first four nights, then an eight night gap after the next three nights, with regular spacing after that. These observational gaps, corresponding to two and three rotation cycles, respectively, did not significantly affect our ability to model surface features and magnetic fields (see Section 4), and only became significant when applying our RV filtering technique (as discussed in Section 5).

All polarization spectra consist of four individual sub-exposures (each lasting 946.2 s for Par 1379, and 835 s for Par 2244), taken in different polarimeter configurations to allow the removal of all spurious polarization signatures at first order. All raw frames were processed using the ESPRIT software package, which performs bias subtraction, flat fielding, wavelength calibration and optimal extraction of (un)polarized échelle spectra, as described in the previous papers of the series (Donati et al. 1997, also see Donati et al. 2010b, 2011, 2014), to which the reader is referred for more information.

Table 1. Journal of ESPaDOnS observations of Par 1379 (first 10 lines) and Par 2244 (last 14 lines). Each observation consists of a sequence of 4 sub-exposures, each lasting 946.2 s for Par 1379 and 835 s for Par 2244, respectively. Columns 1–4 list (i) the UT date of the observation, (ii) the corresponding UT time at mid exposure, (iii) the Barycentric Julian Date (BJD) and (iv) the peak S/N (per 2.6 km s^{-1} velocity bin) of each observation. Columns 5 and 6, respectively, list the S/N in Stokes *I* least-squares deconvolution (LSD) profiles (per 1.8 km s^{-1} velocity bin), and the rms noise level (relative to the unpolarized continuum level I_c and per 1.8 km s^{-1} velocity bin) in the Stokes *V* LSD profiles. Column 7 indicates the rotational cycle associated with each exposure, using the ephemerides given in equation (1).

Date	UT (hh:mm:ss)	BJD (2,456,660+)	S/N	S/N_{LSD}	σ_{LSD} (0.01 per cent)	Cycle
2014 January 07	10:29:51	5.94192	119	1484	5.6	0.011
2014 January 08	10:36:33	6.94653	129	1518	5.1	0.191
2014 January 09	08:44:42	7.86883	122	1521	5.5	0.356
2014 January 10	09:56:19	8.91852	132	1559	4.9	0.544
2014 January 15	10:25:58	13.93888	99	1459	7.1	1.443
2014 January 16	08:49:59	14.87218	122	1521	5.4	1.610
2014 January 17	08:01:30	15.83846	130	1518	5.0	1.783
2014 January 18	09:36:06	16.90410	132	1511	5.0	1.974
2014 January 19	07:37:37	17.82177	113	1466	6.1	2.139
2014 January 20	08:14:06	18.84704	139	1563	4.5	2.322
2014 December 18	13:57:57	351.06756	125	1651	6.0	0.031
2014 December 19	11:52:09	351.98019	126	1638	5.6	0.355
2014 December 20	11:13:19	352.95321	154	1723	4.3	0.701
2014 December 21	12:06:11	353.98993	146	1682	4.7	1.069
2014 December 27	13:45:41	360.05892	96	1260	8.3	3.225
2014 December 28	11:33:31	360.96712	164	1755	4.0	3.547
2014 December 29	10:10:49	361.90967	160	1736	4.2	3.882
2015 January 06	11:15:31	369.95436	141	1685	4.9	6.739
2015 January 07	10:16:28	370.91331	144	1660	4.8	7.080
2015 January 08	10:10:47	371.90933	157	1739	4.1	7.434
2015 January 09	10:12:45	372.91066	139	1682	4.9	7.790
2015 January 10	11:56:48	373.98288	151	1597	4.6	8.170
2015 January 11	10:07:39	374.90704	159	1770	4.1	8.499
2015 January 13	12:22:31	377.00060	138	1622	5.3	9.242

The peak signal-to-noise ratios (S/N; per 2.6 km s^{-1} velocity bin) achieved on the collected spectra range between 99 and 139 (median 126) for Par 1379, and between 96 and 164 (median 145) for Par 2244, depending mostly on weather/seeing conditions. All spectra are automatically corrected for spectral shifts resulting from instrumental effects (e.g. mechanical flexures, temperature or pressure variations) using atmospheric telluric lines as a reference. This procedure provides spectra with a relative RV precision of better than 0.030 km s^{-1} (e.g. Moutou et al. 2007; Donati et al. 2008). A journal of all observations is presented in Table 1 for both stars.

3 STELLAR AND DISC PROPERTIES

Both stars, belonging to the Orion Nebula Cluster (ONC) flanking fields (Fűrész et al. 2008; Tobin et al. 2009), were classified as wTTSs by Rebull et al. (2000) due to their young age (based on evolutionary tracks), combined with a lack of UV excess (suggesting low levels of accretion). Indeed, our spectra show strong, non-variable Li I 6708 Å absorption, confirming the young ages of these targets, with the lack of significant veiling supporting their status as wTTSs (see Section 3.3 for further discussion). Moreover, Rebull (2001) report very regular periodic light curves for both Par 1379 and Par 2244 that do not appear like that of a cTTS, further supporting their non-accreting status. However, Megeath et al. (2012) place Par 1379 near the limit between wTTSs and cTTSs (based on mid-infrared photometry).

Photometric rotation periods of 5.620 ± 0.009 d and 2.820 ± 0.002 d were determined by Rebull (2001) for Par 1379 and Par 2244, respectively, with Carpenter, Hillenbrand & Skrutskie (2001) finding a similar period of 2.83–2.84 d for Par 2244. For the remainder of this work, however, we adopt the rotation periods that are determined from our tomographic modelling in Section 4. Here, the equatorial rotational cycles of Par 1379 and Par 2244 (denoted E_1 and E_2 in equation 1) are computed from Barycentric Julian Dates (BJDs) according to the (arbitrary) ephemerides

$$\begin{aligned} \text{BJD (d)} &= 2456665.9 + 5.585E_1 (\text{for Par 1379}), \\ \text{BJD (d)} &= 2457011.0 + 2.8153E_2 (\text{for Par 2244}), \end{aligned} \quad (1)$$

where our rotational periods are in excellent agreement (within 1 and 2σ of our values) with those determined previously by Rebull (2001) and Carpenter et al. (2001).

3.1 Stellar properties

We applied our automatic spectral classification tool (discussed in Donati et al. 2012) to several of the highest S/N spectra for both stars. This tool is similar to that of Valenti & Fischer (2005), and fits the observed spectrum using multiple windows in the wavelength ranges of 515–520 nm and 600–620 nm, using Kurucz model atmospheres (Kurucz 1993). This process yields estimates of $T_{\rm eff}$ and $\log g$, where the optimum parameters are those that minimize χ^2, with errors bars determined from the curvature of the χ^2 landscape at the derived minimum. For Par 1379, we find that $T_{\rm eff} = 4600 \pm 50$ K

and $\log g = 3.9 \pm 0.2$ (with g in cgs units). Likewise, for Par 2244 we find that $T_{\rm eff} = 4650 \pm 50$ K and $\log g = 4.1 \pm 0.2$.

Our derived $T_{\rm eff}$ is a good estimate in the approximation of a homogeneous star, however, there are likely large ranges in temperature across the photospheres of both stars, given the high level of spot coverage (see Section 4). A two-temperature model would provide a better $T_{\rm eff}$ estimate of the immaculate photosphere, as well as the level of spot coverage (see Gully-Santiago et al. 2017); however, a homogeneous model is sufficient for our purposes.

Given the measured V magnitude of 12.8 for both stars, reported by Rebull et al. (2000), and taking into account a spot coverage of the visible stellar hemisphere of ∼20 per cent (as is typical for active stars, see Section 4), we derive unspotted V magnitudes of 12.6 ± 0.2 for both stars. We note that assuming a different spot coverage (such as 0 or 30 per cent) places our derived parameters within our quoted error bars.

Combining our spectroscopic $T_{\rm eff}$ with the intrinsic colour and $T_{\rm eff}$ sequence for young stars found by Pecaut & Mamajek (2013), we find $(V - I_{\rm C})_0$ to equal 1.09 and 1.07 for Par 1379 and Par 2244, respectively. Using the standard V band extinction of $A_{\rm V} = 3.1E(B - V)$, combined with the conversion of $E(V - I_{\rm C}) = 1.25E(B - V)$ from Bessell & Brett (1988), and the measured colours of $V - I_{\rm C}$ (equal to 1.28 and 1.52), we determine $A_{\rm V}$ to be 0.5 ± 0.2 and 1.1 ± 0.2, for Par 1379 and Par 2244, respectively. Given that we directly measure the spectroscopic temperature, our extinction values are more accurate than those found using colours alone by Rebull et al. (2000) (equal to 0.2 and 0.23).

Using the visual bolometric correction $BC_{\rm v}$ expected at these temperatures (equal to -0.57 ± 0.04 and -0.53 ± 0.03, Pecaut & Mamajek 2013), combined with $A_{\rm V}$, and the trigonometric parallax distance to the ONC of 388 ± 5 pc (corresponding to a distance modulus of 7.94 ± 0.03, Kounkel et al. 2017), we obtain absolute bolometric magnitudes of 3.6 ± 0.3 and 3.0 ± 0.3, or equivalently, logarithmic luminosities relative to the Sun of 0.45 ± 0.11 and 0.72 ± 0.11, for Par 1379 and Par 2244, respectively. When combined with the photospheric temperature obtained previously, we obtain radii of 2.7 ± 0.2 and 3.5 ± 0.2 $R_\odot$.

Coupling the rotation periods of 5.585 d and 2.8153 d for Par 1379 and Par 2244, respectively (see equation 1), with the measured line-of-sight projected equatorial rotation velocity $v \sin i$ of 13.7 ± 0.1 and 57.2 ± 0.1 km s^{-1} (as determined from our tomographic modelling in Section 4), we can infer that $R_\star \sin i$ is equal to 1.52 ± 0.04 and 3.17 ± 0.02 $R_\odot$, where $R_\star$ and i denote the stellar radius and the inclination of its rotation axis to the line of sight. By comparing the radii derived from the luminosities, to that from the stellar rotation, we derive that i is equal to 35° and 64° (to an accuracy of ≃10°) for Par 1379 and Par 2244, respectively.

Using the evolutionary models of Siess, Dufour & Forestini (2000) (assuming solar metallicity and including convective overshooting), we find that the stellar masses are 1.6 ± 0.1 and 1.8 ± 0.1 $M_\odot$, with ages of 1.8 ± 0.6 and 1.1 ± 0.3 Myr, for Par 1379 and Par 2244, respectively (see the H–R diagram in Fig. 1, with evolutionary tracks and corresponding isochrones). However, using the most recent evolutionary models of Baraffe et al. (2015), we obtain substantially different stellar masses of 1.3 ± 0.1 and 1.4 ± 0.1 $M_\odot$, with ages of 1.0 ± 0.5 and 0.5 ± 0.5 Myr, for Par 1379 and Par 2244, respectively. Given the inherent limitations of these evolutionary models, we do not consider the formal error bars on the derived masses and ages to be representative of the true uncertainties, and thus both parameters may be considered to be similar for each star. However, we note that for internal consistency with previous MaPP and MaTYSSE results, the values from the Siess et al. (2000) models should be referenced. We also note that the ages implied by both the Siess et al. (2000) and Baraffe et al. (2015) evolutionary models are somewhat lower than the mean age of the ONC of 2.2 ± 2 Myr, but are still within the spread of ages (Reggiani et al. 2011).

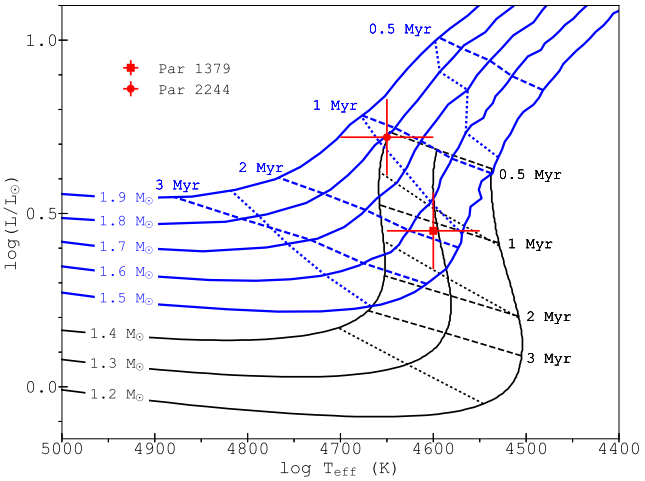

Figure 1. H–R diagram showing the stellar evolutionary tracks provided by Siess et al. (2000, blue solid lines) for masses in the range of 1.5–1.9 $M_\odot$, and those provided by Baraffe et al. (2015, black solid lines) for masses in the range of 1.2–1.4 $M_\odot$. Dashed lines show the corresponding isochrones for ages 0.5, 1, 2 and 3 Myr (blue for Siess et al. 2000 and black for Baraffe et al. 2015). Dotted lines mark the 0, 30 and 50 per cent fractional radius for the size of the radiative core (black for Baraffe et al. 2015) and the bottom of the convective envelope (blue for Siess et al. 2000).

As well as placing the stars at younger ages, with lower masses, the internal structure is also somewhat different between these two evolutionary models, as can be seen in Fig. 1. Here, the size of the convective envelope (by radius) for the Siess et al. (2000) models is around 70 per cent for both stars, whereas the Baraffe et al. (2015) models suggest both stars are fully convective. The most critical change in large-scale magnetic field topology is expected to occur when the star evolves from one that is largely convective, to one that is largely radiative (>50 per cent by radius, depending on the stellar evolution model; e.g. Gregory et al. 2012). Given that the observed field topologies for both stars show non-axisymmetric, mid-to-weak strength poloidal fields (see Section 4.2), the models of Siess et al. (2000) place the stars in better agreement with expectations. Furthermore, the weaker field strength and higher differential shear (see Section 4.3) of Par 1379 suggest that it is likely more structurally evolved than Par 2244, possibly to the point of being mostly radiative (despite the model predictions), whereas Par 2244 is still in a largely convective state.

A more complete study of the change in magnetic topology with internal structure will be performed for the wTTSs in the MATYSSE sample in a future publication, where we will also discuss the implications for different evolutionary models.

3.2 Spectral energy distribution fitting

3.2.1 Model and grid description

Spectral energy distributions (SEDs) of Par 1379 and Par 2244 were constructed using photometric data collected by Rebull et al. (2000), Megeath et al. (2012) and Zacharias et al. (2015) as well as from the *WISE*, *Spitzer* and *Gaia* catalogues (Wright et al. 2010; Werner et al. 2004; Gaia Collaboration et al. 2016). Deep, sensitive

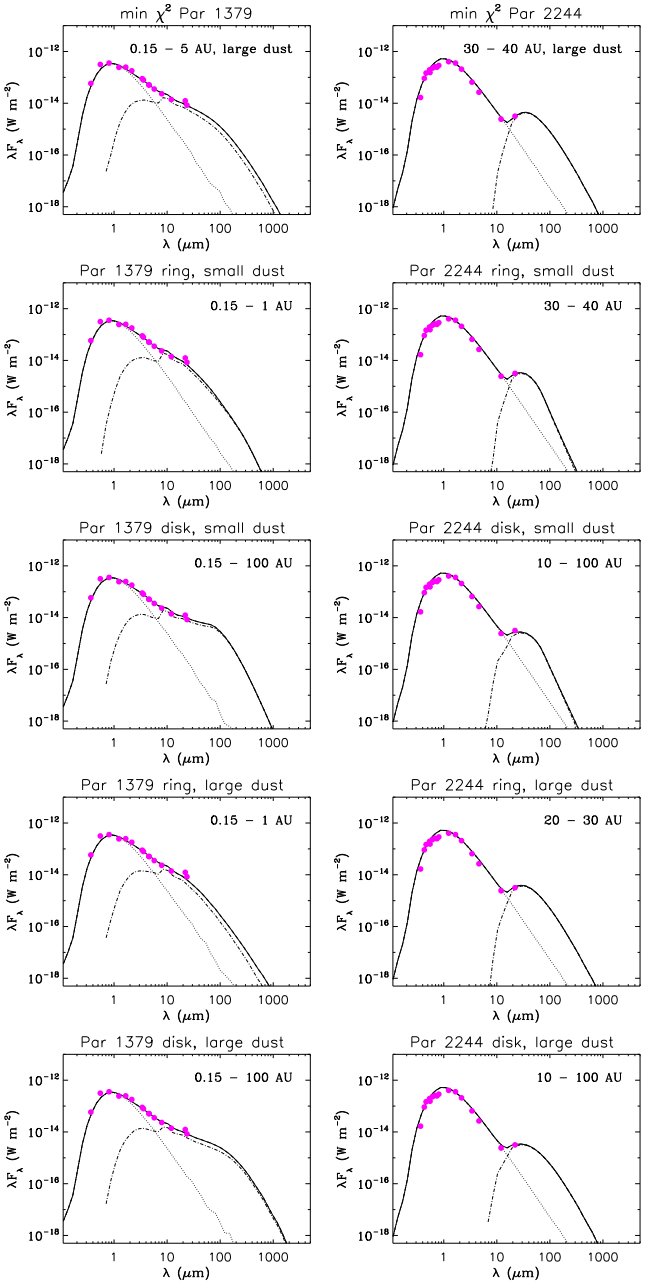

Figure 2. SEDs of Par 1379 (left-hand panels) and Par 2244 (right-hand panels). Photometric points are shown as dots, with the emission from the star marked as a dotted line, the thermal emission from the dust grains inside the disc marked as a dashed-dotted line, and the total marked with a solid line. The models of best fit are shown in the top row, with examples of data-compatible ring models (second and fourth rows) and disc models (third and fifth rows) for both *small dust* and *large dust*.

sub-mm and mm photometries are not currently available for the sources. The SEDs reveal that Par 1379 has an infrared excess starting at 2 μm and that Par 2244 has an infrared excess starting at 22 μm, indicating that both objects have dusty circumstellar discs (see Fig. 2).

To constrain the basic physical properties of the discs, we fit the SEDs using a passively irradiated dusty disc model. For the modelling, we used the stellar properties derived earlier (in Section 3.1), a parametric disc geometry, and to calculate the disc continuum emission, the Monte Carlo dust-radiative transfer code

Table 2. Free parameters explored in the grid of SEDs calculated for Par 1379 (top) and Par 2244 (bottom).

	Par 1379
Dust size (μm)	0.01−10 (small), 0.01−2000 (large)
$R_{\rm in}$ (au)	0.15, 0.2, 0.5, 1, 5, 10, 20
$R_{\rm out}$ (au)	0.5, 1, 5, 10, 20, 30, 50, 100
$M_{\rm dust}$	$10^{-7}, 10^{-6}, 5\times10^{-6}, 10^{-5}$
h_0/r_0	0.01, 0.02, 0.03, 0.05
α	−1.2, −1.0, −0.6
β	1.1
Models	**3936**
	Par 2244
Dust size (μm)	0.01−10 (small), 0.01−2000 (large)
$R_{\rm in}$ (au)	1, 5, 10, 20, 30, 40
$R_{\rm out}$ (au)	5, 10, 20, 30, 40, 50, 100
$M_{\rm dust}$	$10^{-9}, 5\times10^{-9}, 10^{-8}, 5\times10^{-8}, 10^{-7}$
h_0/r_0	0.01, 0.03, 0.05
α	−1.2, −0.6, 0.0
β	1.1
Models	**2430**

Note. α corresponds to the exponent of the surface density power law, and β to the exponent of the disc flaring and $r_0 = 1$ au.

MCFOST (Pinte et al. 2006, 2009). The parametric disc model has a flared geometry with a Gaussian density profile in the vertical direction $\rho(r, z) = \rho(r)\exp(-z^2/2h(r)^2)$. The dust surface density distribution and the scaleheight as a function of the radius are described with power laws $\Sigma(r) = \Sigma_0(r/r_0)^\alpha$ and $h(r) = h_0(r/r_0)^\beta$, respectively, where h_0 is the scaleheight at the reference radius r_0. The value of Σ_0 is deduced from the assumed disc dust mass $M_{\rm dust}$. The free parameters for computing a model are therefore the dust size distribution and composition, the disc inner radius $R_{\rm in}$, the disc outer radius $R_{\rm out}$, the dust disc mass $M_{\rm dust}$, the aspect ratio h_0/r_0, the flaring angle β and the surface density exponent α.

We assumed astronomical silicate opacities for the dust (Draine & Lee 1984) and tested models with two dust size distributions: a *small dust* distribution with 0.01–10 μm sized grains, and a *large dust* distribution with 0.01–2000 μm grains, assuming a size distribution slope of 3.5 for both distributions. We used a reference radius r_0 of 1 au and a flaring angle β of 1.1. Furthermore, we assumed disc inclinations of 36° and 59° for Par 1379 and Par 2244, respectively (from our tomographic modelling in Section 4), and a distance of 388 pc for both objects.

For each of the sources, we ran a uniform grid of SED models, varying the free parameters as described in Table 2. The grid includes *disc-like* models extending tens to hundreds of au and narrow *ring-like* models with a width of a few au. In total, we tested 3936 models for Par 1379 and 2430 models for Par 2244. For each SED model, the χ^2 statistic was computing using the logarithm of the flux in each photometric band. Each χ^2 lead to a model probability defined as $P = \exp(-\chi^2/2)$. The ensemble of probabilities P of the grid were normalized such that the sum of P in the entire grid is equal to 1. Armed with the probability for each model in the grid, we constructed histograms for each free parameter, by summing P over all models in the grid that had the same value of the free parameter. In the case of $R_{\rm in}$ and $R_{\rm out}$, for calculating the histograms, the sum of P in each histogram bin was divided by the number models in that bin, and the histograms were re-normalized such that their sum is equal to 1. This was necessary because models with $R_{\rm out} < R_{\rm in}$ are not possible, and the histograms need to be corrected for the different number of models per bin. Additionally, in the case of $R_{\rm in}$

Table 3. Examples of models describing the SEDs of Par 1379 (top) and Par 2244 (bottom).

Model	min χ^2	Ring	Disc	Ring	*Disc*
Dust size	Large	Small		Large	
		Par 1379			
$R_{\rm in}$ (au)	0.15	0.15	0.15	0.15	0.15
$R_{\rm out}$ (au)	5	1	100	1	100
h_0/r_0	0.03	0.03	0.03	0.03	0.03
$M_{\rm dust}$ (10^{-6} $M_\odot$)	1	0.1	5	1.0	10
α	−1.0	−0.6	−1.2	−1.2	−1.2
β	1.1	1.1	1.1	1.1	1.1
		Par 2244			
$R_{\rm in}$ (au)	30	30	10	20	10
$R_{\rm out}$ (au)	40	40	100	30	100
h_0/r_0	0.03	0.03	0.01	0.01	0.03
$M_{\rm dust}$ (10^{-8} $M_\odot$)	10	0.5	1	5	10
α	−1.2	−0.6	0.0	−1.2	−0.6
β	1.1	1.1	1.1	1.1	1.1

Note: α corresponds to the exponent of the surface density power law and β to the exponent of the disc flaring, and $r_0 = 1$ au.

and $R_{\rm out}$, and $M_{\rm dust}$ and $R_{\rm out}$, we constructed 2D χ^2 plots to reveal cross-correlations between these parameters.

3.2.2 *SED-fitting results*

Our results are summarized in Figs 2 and B1 and Table 3. Ring and disc solutions describe the SED equally well, highlighting that the solutions are degenerate. Indeed, to better distinguish between the models, one would require sensitive sub-mm and mm photometry as well as spatially resolved imaging. However, despite the degeneracies, we may draw general conclusions given that the near-IR SED enable us to constrain the inner radius of the IR-excess emission, as well as the disc's scaleheight (if the emission is optically thick). Furthermore, the SED provides us with an order-of-magnitude estimate of the dust mass, given a disc's geometry and extension.

In the case of Par 1379, the near-IR excess requires the presence of warm dust at $R < 1$ au. The probability histogram (Fig. B1) clearly displays a higher probability for models with inner radius 0.15 and 0.2 au. The outer disc is less well constrained, but there is a preference for models with an outer disc radius smaller than 10 au. The solution with the minimum χ^2 has $R_{\rm in} = 0.15$ au and $R_{\rm out} = 5$ au. However, one should bear in mind that the preference for discs with an outer radius smaller than 10 au in the grid could be a bias due to the absence of sensitive sub-mm photometry. The SED could in fact be explained either by a narrow, low-mass (10^{-7} $M_\odot$) ring of warm dust between 0.15 and 1 au, a disc with mass 10^{-6} $M_\odot$ extending from 0.15 to 10 au, or a large 100 au disc with a dust mass of 10^{-5} $M_\odot$ (note that in Fig. B1, for $R_{\rm in} = 0.15$ au, the probability of models with $R_{\rm out} > 2$ au is similar). Large and dust grain distributions appear to have similar probabilities, and the dust surface density exponent is not well constrained, as all the values in the grid display a similar probability. However, the model with the minimum χ^2 has a dust distribution with large grains, and a dust mass of 10^{-6} $M_\odot$ with $\alpha = -1.0$.

Compared with the dust mass measured in the discs of cTTSs in Taurus (10^{-6}–10^{-4} $M_\odot$, Andrews & Williams 2005), Par 1379 has a lower dust mass than a typical cTTS, if the disc of Par 1379 is smaller than 10 au. However, if the disc of Par 1379 is large, then its dust mass would be comparable to those of standard cTTS discs. The scaleheight h/r required to fit the SED of Par 1379 is between 0.02 and 0.03 at 1 au – a value similar to the scaleheight of 0.03 of an isothermal disc in hydrostatic equilibrium around a 1.6 $M_\odot$ star at 1 au, assuming a mid-plane temperature of 350 K.[1] The scaleheight suggested by the SED fit indicates that some gas might be still present in the disc. In summary, the SED of Par 1379 suggests that it is surrounded by a dusty disc extending down to the silicate sublimation radius and that this disc is likely primordial as its scaleheight is consistent with a disc in hydrostatic equilibrium.

In the case of Par 2244, the SED fit reveals that there is an inner dust cavity of at least 10 au in radius, with the models that best describe the data possessing an inner radii of 20 au. Dusty rings around 20–30 au with a width of 10–20 au have higher probabilities in the grid; however, a dust disc extending 10–100 au can also satisfactorily describe the data. The model with the lowest χ^2 is a dusty ring extending from 30 to 40 au, with a dust mass of 10^{-7} $M_\odot$ and large dust grains. However, a similar model with a small dust distribution and a mass of 5×10^{-9} $M_\odot$ describes the data equally well. The lack of sensitive sub-mm photometry limits our ability to distinguish between these two models, however, in the whole ensemble of the grid there is the statistical trend that the models that best reproduce the SED have dust masses of 10^{-9}–10^{-8} $M_\odot$, which are very low masses, when compared to the mass of cTTS in Taurus. The low dust mass suggested by the SED fit (solutions are optically thin) together with the lack of strong accretion signatures (see Section 3.3) hints that Par 2244 has either recently dissipated its gaseous disc and we only observe the remaining primordial dust, or alternatively, that Par 2244 harbours a young debris disc. We note, however, that the grid slightly favours large grain solutions, lending weight to the hypothesis of remaining primordial dust. As the solutions are optically thin, stringent constraints on the scaleheight and surface density exponent cannot be derived. In summary, the SED suggests that Par 2244 is surrounded by a low mass 10^{-9}–10^{-8} $M_\odot$ dusty disc, extending at least to 50 au with a 10–20 au cavity. Par 2244 could be considered as a non-accreting transition disc, or a young-debris disc.

Given that we detect discs around both our target stars, we may estimate the age at which disc locking ceased by assuming a disc-locking period of 6–12 d (for stars with $M > 0.3$ $M_\odot$, see Landin et al. 2016) with constant angular momentum evolution since then. Given these assumptions, we find ages around 0.7–1.50 and 0.3–0.5 Myr for Par 1379 and Par 2244, respectively (using Siess et al. 2000 evolutionary tracks). These ages are consistent with typical disc dissipation time-scales of $\simeq$1 Myr for the ONC (ranging between 0.2 and 3 Myr, see Landin et al. 2016), with Par 2244 in particular dissipating its disc at a relatively young age. For the Baraffe et al. (2015) evolutionary models, we are only able to place upper limits of 0.5 Myr on the age at which disc locking ceased, for both stars.

3.3 Accretion status

The presence of dusty discs in Par 1379 and Par 2244 raises the question of whether the discs still have gas, and whether the stars are still accreting. Given that we have obtained multiple high-quality spectra of both targets, we may determine their accretion status using several metrics.

[1] $h/r = c_s/v_K = \sqrt{\frac{k_{\rm B}T}{\mu m_{\rm H}} \frac{r}{GM_\star}}$, where c_s is the sound speed, v_K is the Keplerian velocity, $k_{\rm B}$ is the Boltzmann constant, μ is the mean molecular weight (2.3), $m_{\rm H}$ is the proton mass, r is the radius and G is the gravitational constant.

Table 4. Main parameters of Par 1379 and Par 2244 as derived from our study (plus their distance), with $v_{\rm rad}$ noting the RV that the star would have if unspotted (as inferred from the modelling of Section 4). Note, the stellar masses and ages are those determined from Siess et al. (2000) models, with values from Baraffe et al. (2015) given in parenthesis.

	Par 1379	Par 2244
$M_\star$ ($M_\odot$)	1.6 ± 0.1 (1.3 ± 0.1)	1.8 ± 0.1 (1.4 ± 0.1)
$R_\star$ ($R_\odot$)	2.7 ± 0.2	3.5 ± 0.2
age (Myr)	1.8 ± 0.6 (1.0 ± 0.5)	1.1 ± 0.3 (0.5 ± 0.5)
$\log g$ (cgs units)	3.9 ± 0.2	4.1 ± 0.2
$T_{\rm eff}$ (K)	4600 ± 50	4650 ± 50
$\log(L_\star/L_\odot)$	0.45 ± 0.11	0.72 ± 0.11
$P_{\rm rot}$ (d)	5.585 ± 0.035	2.8153 ± 0.0023
$v \sin i$ (km s^{-1})	13.7 ± 0.1	57.2 ± 0.1
$v_{\rm rad}$ (km s^{-1})	30.40 ± 0.07	27.00 ± 0.05
i (°)	$36° \pm 10°$	$59° \pm 10°$
Distance (pc)	388 ± 5	388 ± 5

We find that both Par 1379 and Par 2244 show core Ca II infrared triplet (IRT) emission, with mean equivalent widths (EWs) of around 0.44 Å (15.5 km s^{-1}) and 0.20 Å (7.3 km s^{-1}), similar to what is expected from chromospheric emission for such PMS stars, and somewhat lower than that for accreting cTTSs (e.g. Donati et al. 2007). We also find that both Par 1379 and Par 2244 show Hα, Hβ and He I D_3 emission, with Par 1379 in particular displaying a time-varying absorption component in both Hα and Hβ.

One may estimate the level of surface accretion in TTSs by adopting the relations between line luminosity $L_{\rm line}$ and the accretion luminosity $L_{\rm acc}$ of Alcalá et al. (2017). For this purpose, we determined $L_{\rm line}$ by assuming blackbody scaling using the stellar radius $R_\star$ and $T_{\rm eff}$ given in Table 4. Then, following Gullbring et al. (1998), the mass accretion rate $\dot{M}_{\rm acc}$ was calculated using the relationship

$$\dot{M}_{\rm acc} = \frac{L_{\rm acc} R_\star}{G M_\star (1 - \frac{R_\star}{R_{\rm in}})}, \quad (2)$$

where $R_{\rm in}$ denotes the truncation radius of the disc, and is taken to be $5R_\star$ (Gullbring et al. 1998).

For Par 1379, we detect weak He I D_3 emission, with an EW of around 0.012 Å (0.6 km s^{-1}), corresponding to $\log \dot{M}_{\rm acc} \simeq -10.7$ $M_\odot$ yr^{-1}. For Hβ, we detect absorption components in several line profiles between phases 0–0.4 (see Fig. A1), and we find the EW of the Hβ emission to range between 0.01 and 0.34 Å (average of 0.16 Å, equivalent to 9.8 km s^{-1}, corresponding to $\log \dot{M}_{\rm acc} \simeq -10.6$ $M_\odot$ yr^{-1}). Moreover, we detect a redshifted absorption component (in addition to the emission) in several Hα line profiles between phases 0.0 and 0.4 (see Fig. A1). We find the EW of the emission ranges between 1.4 and 3.6 Å (average of 2.4 Å, equivalent to 108 km s^{-1}, corresponding to $\log \dot{M}_{\rm acc} \simeq -9.9$ $M_\odot$ yr^{-1}), and that of the absorption ranges between 0.1 and 1.4 Å (average of 0.5 Å, equivalent to 24 km s^{-1}). In the case of Par 2244, we detect very weak He I D_3 emission, with an EW of around 0.005 Å (0.25 km s^{-1}), corresponding to $\log \dot{M}_{\rm acc}$ of around -11.1 $M_\odot$ yr^{-1}. Furthermore, we find weak Hβ emission, with an average EW of 0.06Å (3.7 km s^{-1}, corresponding to $\log \dot{M}_{\rm acc} \simeq -10.9$ $M_\odot$ yr^{-1}). Moreover, we do not find any absorption in the Hα profiles of Par 2244, with the mean emission EW of 1.3Å (60 km s^{-1}, corresponding to $\log \dot{M}_{\rm acc} \simeq -10.1$ $M_\odot$ yr^{-1}, see Fig. A1).

At such low EWs and accretion rates, chromospheric activity becomes a significant influence on the strength and width of emission lines (Ingleby et al. 2011). For TTSs in particular, their large convective turnover times (Gilliland 1986) combined with their rapid rotation means they possess a low Rossby number, placing them well within the saturated activity regime (e.g. Reiners, Schüssler & Passegger 2014). For young stars, the Hα line luminosity is observed to saturate at around $\log[L(\mathrm{H}\alpha)/L_{\rm bol}] = -3.3$ or lower (around -3.8 for K4 spectral types, Barrado y Navascués & Martín 2003; around -4.0 for later spectral types, see Newton et al. 2017). As our target stars both show line luminosities below these levels, with $\log[L(\mathrm{H}\alpha)/L_{\rm bol}]$ equal to -4.5 for Par 1379 and -5.0 for Par 2244, any measurements of accretion rates based on the line luminosities (especially Hα and to a lesser extent Hβ) must be considered to be significantly influenced or even dominated by chromospheric activity.

The limit at which one can distinguish between accretion and chromospheric activity has been explored by several authors. Barrado y Navascués & Martín (2003) propose a spectral-type dependant relationship between the EW(Hα) and the accretion rate. Their empirical criterion is based on the saturation limit of chromospheric activity (taken to be $\log[L(\mathrm{H}\alpha)/L_{\rm bol}] = -3.3$) and is used to distinguish between accreting and non-accreting stars and brown dwarfs.

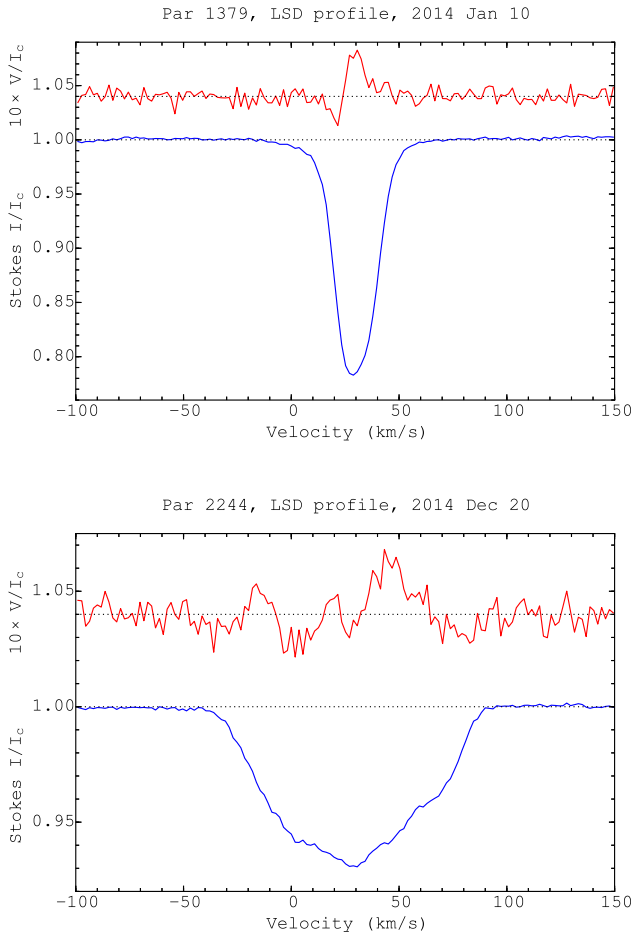

Figure 3. LSD circularly-polarized (Stokes *V*, top/red curve) and unpolarized (Stokes *I*, bottom/blue curve) profiles of Par 1379 (top panel) and Par 2244 (bottom panel) collected on 2014 January 10 (cycle 0.54) and 2014 December 20 (cycle 0.7). Clear Zeeman signatures are detected in the LSD Stokes *V* profile of both stars in conjunction with the unpolarized line profiles. The mean polarization profiles are expanded by a factor of 10 and shifted upwards by 1.04 for display purposes.

Adopting the spectral type of K4 for both Par 1379 and Par 2244, as determined from our spectroscopic temperature in Section 3.1, the criterion of Barrado y Navascués & Martín (2003) defines a cTTS threshold of EW(Hα) = 4.4 Å. Given that the EW(Hα) of both Par 1379 and Par 2244 are below these limits (with maxima of 3.6 and 2.1 Å for Par 1379 and Par 2244, respectively), both stars fall into the non-accreting regime (where line broadening is dominated by chromospheric activity).

Elsewhere, the impact of chromospheric activity on accretion rate measurements was explored by Manara et al. (2013), where the authors determined the point at which the line emission may be dominated by the contribution of chromospheric activity (termed chromospheric accretion 'noise'). Using the empirical relationships from Manara et al. (2013), we have determined that the level of chromospheric noise for Par 1379 and Par 2244 is equal to $\log(L_{\rm acc,\,noise}/L_{\rm star}) = -1.9 \pm 0.1$. For Par 1379, the measured line luminosities $\log(L_{\rm acc}/L_{\rm star})$ for Hα, Hβ and He I D_3 are, respectively, equal to -2.3 ± 0.3, -2.9 ± 0.3 and -3.1 ± 0.3. For Par 2244, we find that $\log(L_{\rm acc}/L_{\rm star})$ for Hα, Hβ and He I D_3 are, respectively, equal to -1.9 ± 0.3, -2.0 ± 0.3 and -3.3 ± 0.3. Comparing these values, we see that the luminosity of all three emission lines (for both stars) are significantly below the threshold where the line is dominated by chromospheric emission (apart from Hα and Hβ for Par 2244, which are at a similar level to the chromospheric noise). Thus, the accretion rates determined above for Par 1379 and Par 2244 must be taken to be upper limits, given that chromospheric emission is likely the dominant broadening mechanism. Indeed, Manara et al. (2013) derive a limit for the detectable accretion rate of $\dot{M}_{\rm acc} \sim 3 \times 10^{-10}$ M$_\odot$ yr^{-1} for a 1.1 M$_\odot$ mass star at 3 Myr old (the closest mass and age available for our targets). Moreover, as higher mass stars have a higher detection limit, the fact that our derived $\dot{M}_{\rm acc}$ are lower than this limit indicates that our target stars are likely not accreting, or are accreting at a low (undetectable) level. Thus, as the accretion rates are likely very low, we refer to our target stars as wTTSs.

Given that the Hα emission in our targets is likely dominated by chromospheric emission, it is somewhat unreliable as a classification and accretion diagnostic. Nevertheless, White & Basri (2003) have proposed using the width of Hα emission at 10 per cent intensity to distinguish between cTTSs and wTTSs, with stars possessing a width >270 km s^{-1} classed as cTTSs (also, see e.g. Fang et al. 2009). In the case of Par 1379, we find that the Hα width at 10 per cent intensity ranges between 163 and 313 km s^{-1}, with an average of 226 km s^{-1}, thus placing it well within the wTTS regime (Hα line profiles are shown in Fig. A1). Indeed, only three of the ten spectra show a width above 270 km s^{-1} (at cycles 1.610, 1.783 and 1.974 in Fig. A1). Compared to the average spectrum, these three line profiles are additionally broadened by a blueshifted emission component. This broadening may be related to accretion; however, the blueshifted emission may also be explained by prominences rotating into view (see discussion in Section 6), given the reconstructed magnetic field topology (see Section 4.2). For Par 2244, we find that the Hα width at 10 per cent intensity ranges between 187 and 430 km s^{-1}, with an average of 318 km s^{-1} (see Fig. A1), thus placing it within the cTTS regime. However, its high $v \sin i$ of 57.2 km s^{-1} (see Section 4) additionally broadens the Hα line, and if this and the significant chromospheric emission is accounted for, Par 2244 likely falls below the threshold for accretion.

As well as classing our targets as cTTSs or wTTSs, one may also estimate the mass accretion rate using the Hα width at 10 per cent intensity and the relationship found by Natta et al. (2004). Here, the accretion rate $\log \dot{M}_{\rm acc}$ for Par 1379 ranges between -9.9 and -11.3 M$_\odot$ yr^{-1}, with an average of -10.7 M$_\odot$ yr^{-1}. For Par 2244, the accretion rate ranges between -8.7 and -11.1 M$_\odot$ yr^{-1}, with an average of -9.8 M$_\odot$ yr^{-1}. However, the authors note that, due to the large dispersion, accretion rates derived from this relationship are necessarily inaccurate for individual objects, and so should be used with care. Indeed, given that Hα is likely dominated by chromospheric emission (see discussion above), this method for deriving accretion rates is unreliable.

4 TOMOGRAPHIC MODELLING

Having characterized the atmospheric properties, and the evolutionary and accretion status of Par 1379 and Par 2244, we now apply our dedicated stellar-surface tomographic-imaging package to the spectropolarimetric data set described in Section 2. In using this tool, we assume that the observed variability in the data is dominated by rotational modulation (and optionally differential rotation). Then, the imaging code simultaneously inverts a time series of Stokes I and Stokes V profiles into brightness maps (featuring both cool spots and warm plages, known to contribute to the activity of very active stars) and magnetic maps (with poloidal and toroidal components, using a spherical harmonic decomposition). For brightness imaging, a copy of a local line profile is assigned to each pixel on a spherical grid, and the total line profile is found by summing over all visible pixels (at a given phase), where the pixel intensities are scaled iteratively to fit the observed data. For magnetic imaging, the Zeeman signatures are fit using a spherical-harmonic decomposition of potential and toroidal field components, where the weighting of the harmonics are scaled iteratively (Donati 2001). The data are fit to an aim χ^2, with the optimal fit determined using the maximum-entropy routine of Gull & Skilling (1991), and where the chosen map is that which contains least information (maximum entropy) required to fit the data. For further details about the specific application of our code to wTTSs, we refer the reader to previous papers in the series (e.g. Donati et al. 2010b, 2014, 2015).

Given that typical Zeeman signatures have relative amplitudes of ~0.1 per cent, with relative noise levels of around 10^{-3} in a typical spectrum (for a single line), we require some means to improve the S/N to a sufficient level for reliable mapping of the stellar magnetic fields. To achieve this, least-squares deconvolution (LSD; Donati et al. 1997) was applied to all spectra. This technique involves cross-correlating the observed spectrum with a stellar line-list, and results in a single 'mean' line profile with a dramatically improved S/N, with accurate error bars for the Zeeman signatures (Donati et al. 1997). The stellar line list used for LSD was sourced from the Vienna Atomic Line Database (VALD; Ryabchikova et al. 2015), and was computed for $T_{\rm eff} = 4500$ K and $\log g = 4.0$ (in cgs units), appropriate for both Par 1379 and Par 2244 (see Section 3.1). Only moderate to strong atomic spectral lines were included (with line-to-continuum core depressions larger than 40 per cent prior to all non-thermal broadening). Furthermore, spectral regions containing strong lines mostly formed outside the photosphere (e.g. Balmer, He, Ca II H & K and IRT lines) and regions heavily crowded with telluric lines were discarded (see e.g. Donati et al. 2010b for more details), leaving 6671 spectral lines for use in LSD. Expressed in units of the unpolarized continuum level $I_{\rm c}$, the average noise level of the resulting Stokes V signatures range from 4 to 8.3×10^{-4} per 1.8 km s^{-1} velocity bin, with a median value of 4.9×10^{-4} for both stars.

Zeeman signatures are detected at all times in Stokes V LSD profiles (see Fig. 3 for an example), featuring typical amplitudes

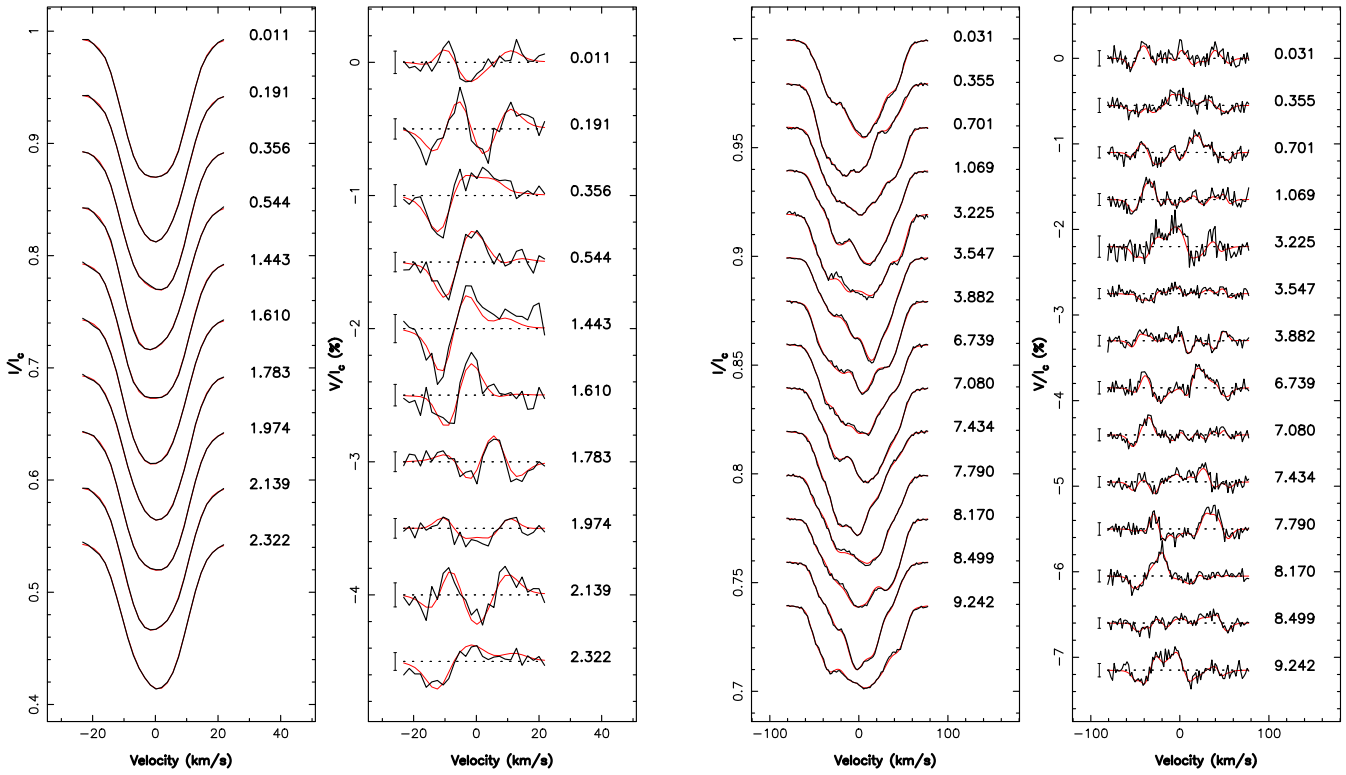

Figure 4. Maximum-entropy fit (thin red line) to the observed (thick black line) Stokes *I* (first and third panels) and Stokes *V* (second and fourth panels) LSD photospheric profiles of Par 1379 (first two panels) and Par 2244 (last two panels). Rotational cycles are shown next to each profile. This figure is best viewed in colour.

of 0.2–0.3 per cent for both Par 1379 and Par 2244, with the latter showing more complex field structures. Distortions are also visible in Stokes *I* LSD profiles for both stars, suggesting the presence of brightness inhomogeneities on the surface of both stars, with the larger distortions for Par 2244 suggesting a higher number of surface structures.

The disc-integrated average photospheric LSD profiles are computed by first synthesizing the local Stokes *I* and *V* profiles using the Unno-Rachkovsky analytical solution to the polarized radiative transfer equations in a Milne-Eddington model atmosphere, taking into account the local brightness and magnetic field. Then, these local line profiles are integrated over the visible hemisphere (including linear limb darkening) to produce synthetic profiles for comparison with observations. This method provides a reliable description of how line profiles are distorted due to magnetic fields (including magneto-optical effects, e.g. Landi Degl'Innocenti & Landolfi 2004). The main parameters of the local line profiles are similar to those used in our previous studies: the wavelength, Doppler width, EW and Landé factor being set to 670 nm, 1.8 km s^{-1}, 3.9 km s^{-1} and 1.2, respectively.

As part of the imaging process, we obtain accurate estimates for $v_{\rm rad}$ (the RV of the star would have if unspotted) equal to 30.40 ± 0.07 and 27.00 ± 0.05 km s^{-1}, the $v \sin i$ equal to 13.7 ± 0.1 and 57.2 ± 0.1 km s^{-1}, and the inclination i of the rotation axis to the line of sight equal to $36^\circ \pm 10^\circ$ and $59^\circ \pm 10^\circ$ (in excellent agreement with the values derived in Section 3.1) for Par 1379 and Par 2244, respectively (see Table 4).

4.1 Brightness and magnetic imaging

Fig. 4 shows the Stokes *I* and *V* LSD profiles of Par 1379 and Par 2244, as well as our fits to the data. All our fits correspond to a reduced chi-squared $\chi^2_{\rm r}$ equal to 1 (i.e. where χ^2 equals the number of fitted data points, equal to 260 for Par 1379, and 1246 for Par 2244), emphasizing the high quality of our data set and our modelling technique at reproducing the observed modulation of the LSD profiles. While the phase coverage for our two stars is less dense than that for LkCa 4, V819 Tau or V830 Tau (see Donati et al. 2014, 2015), the small rms of the RV residuals for both stars (see Section 5) and the large $v \sin i$ for Par 2244 (providing $\sim$4$\times$ the resolution compared to Par 1379), means we can safely claim that our maps include no major imaging artefact nor bias.

The brightness maps of Par 1379 and Par 2244 include both cool spots and warm plages (see Fig. 5), with Par 2244 showing significantly more contrast between these features. The brightness map of Par 1379 features a single dark, circular spot over the polar region, with a region of bright plage extending from around 70° to the equator (centred around phase 0.65). These relatively simple features are required to reproduce the observed Stokes *I* profile distortions for Par 1379 (concentrating in the line cores rather than in the wings, see Fig. 4), and in particular, the small RV variations (of maximum amplitude 0.28 km s^{-1}, see Section 5). We find an overall spot and plage coverage of $\simeq$5 per cent ($\simeq$2.5 per cent each for spots and plages), much lower than that for LkCa 4 (Donati et al. 2014), and around half that for V819 Tau and V830 Tau (Donati et al. 2015).

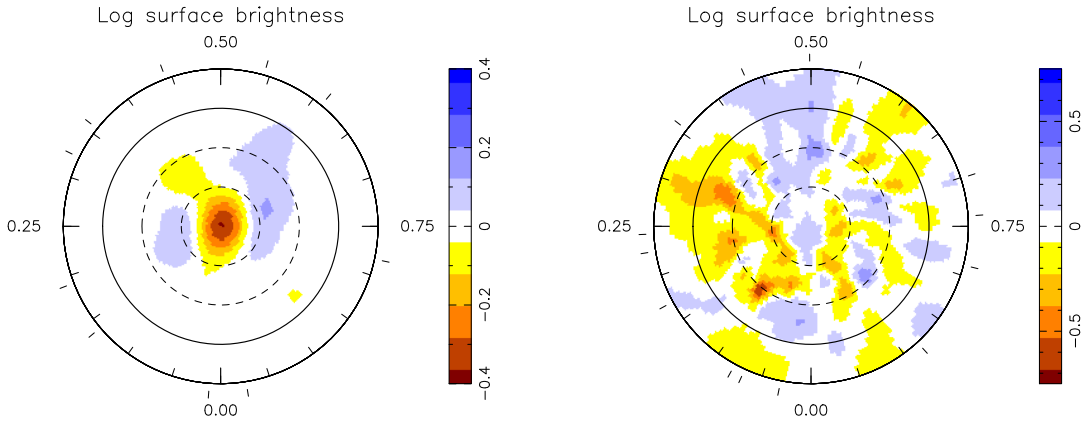

Figure 5. Maps of the logarithmic brightness (relative to the quiet photosphere), at the surfaces of Par 1379 (left) and Par 2244 (right). The stars are shown in flattened polar projection down to latitudes of −30°, with the equator depicted as a bold circle, and 30°and 60° parallels as dashed circles. Radial ticks around each plot indicate phases of observations. This figure is best viewed in colour.

The brightness map of Par 2244 (the right-hand panel of Fig. 5) features spots and plages distributed across the entire surface, with no polar spot. Spotted regions extend from around 70° to below the equator around phase 0.2–0.35, with a region of bright plages extending from the pole to below the equator around phase 0.4–0.5. We find an overall spot and plage coverage of ≃19 per cent (≃11 and ≃8 per cent for spots and plages, respectively), where the numerous and complex surface features are required to fit the large RV fluctuations (of maximum amplitude 5.1 km s^{-1}, see Section 5) of the observed line profiles. We note that the relatively poor fit at cycle 3.225 (providing the largest RV residual, see Fig. 10) coincides with strong, relatively narrow Hα emission (see Fig. A1).

Note that the estimates of spot and plage coverage should be considered as lower limits only, as Doppler imaging is mostly insensitive to small-scale structures that are evenly distributed over the stellar surface (hence the larger minimal spot coverage assumed in Section 3.1 to derive the location of the stars in the H–R diagram).

4.2 Magnetic field imaging

The reconstructed magnetic fields are described as a sum of a poloidal and toroidal fields, each expressed a spherical-harmonic (SH) expansion, with ℓ and m denoting the mode and order of the SH (Donati et al. 2006). For a given set of complex coefficients $\alpha_{\ell,m}$, $\beta_{\ell,m}$ and $\gamma_{\ell,m}$ (where $\alpha_{\ell,m}$ characterizes the radial field component, $\beta_{\ell,m}$ the azimuthal and meridional components of the poloidal field term and $\gamma_{\ell,m}$ the azimuthal and meridional components of the toroidal field term), one can construct an associated magnetic image at the surface of the star, and thus derive the corresponding Stokes V data set. The inverse is carried out here, where we reconstruct the set of coefficients that fit the observed data.

The reconstructed magnetic fields of Par 1379 and Par 2244 (see Fig. 6) are quite different in both strength and topological properties. For Par 1379, the field mainly consists of a mostly non-axisymmetric poloidal component (at a level of 74 per cent). The largest fraction of the reconstructed poloidal field energy (45 per cent) is contained in the quadrupolar ($\ell = 2$) SH mode, with the remainder split evenly between the other modes (i.e. with ℓ =1, 3 and 4). The large-scale topology of the poloidal component is tilted at ≃65° from the rotation axis (towards phase 0.41), and generates an intense radial field in excess of 400 G at mid-latitudes around phase 0.7 (see the top left-hand panel of Fig. 6). We also find a mostly-axisymmetric toroidal component (containing 26 per cent of the total energy), with 44 per cent of the toroidal magnetic energy in the $\ell = 1$ dipole, with a further 33 per cent of the toroidal energy in the $\ell = 4$ mode, combining to producing fields in excess of 400 G at low-to-mid latitudes (see the centre top panel of Fig. 6). In total, we find an unsigned field strength of 250 G.

For Par 2244, the field mainly consists of a mostly non-axisymmetric poloidal component (58 per cent), with 48 per cent of the reconstructed energy contained in modes with $\ell \geq 4$ (with the remaining energy split fairly evenly between modes with $\ell < 4$). The poloidal component can be approximated at large distances from the star by a 330 G dipole tilted at ≃45° from the rotation axis (towards phase 0.57), which when combined with higher order modes generates fields in excess of 1 kG at the surface (see the bottom left-hand panel of Fig. 6). We also find a significant, mostly axisymmetric toroidal component (42 per cent of the total) with ≃31 per cent of the reconstructed energy contained in modes with $\ell = 1$ and 4. This complex topology generates fields in excess of 2 kG at low latitudes (see the bottom-centre panel of Fig. 6). In total, we find an unsigned field strength of 0.86 kG. Comparing the brightness and magnetic maps of Par 2244 (see Figs 5 and 6, respectively), one can see there is some degree of spatial correlation between features. In particular, the moderately strong radial fields (around phases 0.4–0.5), and the strong azimuthal fields at low latitudes (at phases 0.15–0.35 and 0.55–0.65) loosely correlate with the high plage and spot coverage at these phases in the brightness map.

Lastly, we note that the SH expansions describing the reconstructed field presented in Fig. 6 are limited to terms with $\ell \leq 5$ for Par 1379, as only marginal changes to the solution are observed when larger ℓ values are included, indicating that most of the detected Stokes V signal for Par 1379 concentrates at larger spatial scales. In contrast, the SH expansion for Par 2244 requires terms with $\ell \leq 18$ to fit the data to $\chi^2_r = 1$, indicating a more complex and compact magnetic field topology. Given that the amount of reconstructed structure depends on the star's $v \sin i$, we may expect to have around four times the effective resolution for Par 2244 as compared to Par 1379. Thus, to compare like for like, we reconstructed the brightness and magnetic maps for Par 2244 while limiting the number of SH terms to $\ell \leq 5$ (matching that for Par 1379). The resulting maps cannot be fit to the same level of χ^2_r; however, the

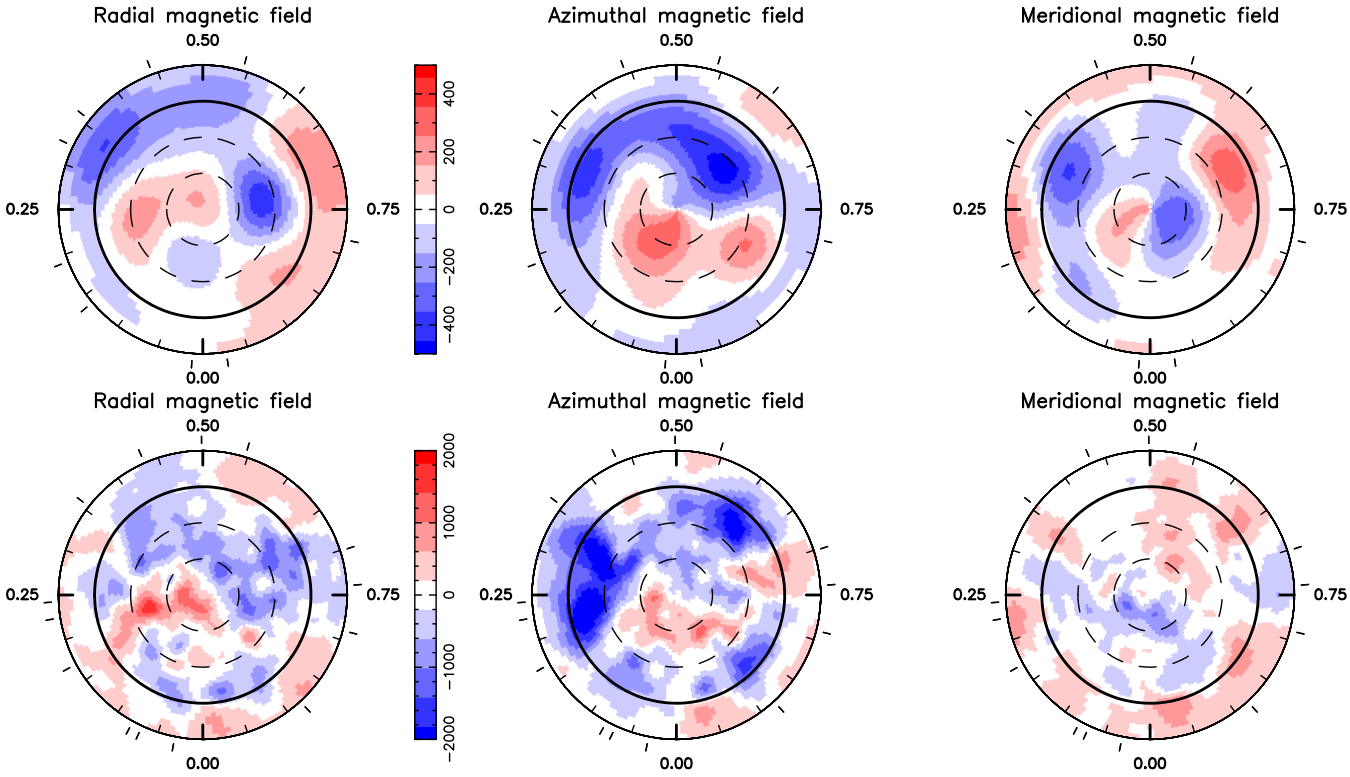

Figure 6. Maps of the radial (left), azimuthal (middle) and meridional (right) components of the magnetic field $\boldsymbol{B}$ at the surfaces of Par 1379 and (top) and Par 2244 (bottom). Magnetic fluxes in the colour bar are expressed in G. The stars are shown in flattened polar projection as in Fig. 5. This figure is best viewed in colour.

resulting topology is very similar to that found when including significantly more terms. We find a mainly non-axisymmetric field split 60:40 between poloidal and toroidal components, with the largest fraction of poloidal energy in the $\ell \geq 4$ modes, and an unsigned field strength around 30 per cent larger. Thus, as the data were fit in the same manner, we confirm that Par 2244 has a significantly more complex field topology compared to Par 1379. This property is also reflected in the Stokes V profiles of Par 2244, as if one degraded them to the same velocity resolution as Par 1379, the Zeeman signatures would be weaker and more complex than those dominating the Stokes V profiles of Par 1379.

In Fig. 7 , we present the extrapolated large-scale field topologies of Par 1379 and Par 2244 using the potential field approximation (e.g. Jardine, Collier Cameron & Donati 2002), and derived solely from the reconstructed radial field components. These potential topologies represent the lowest possible states of magnetic energy and provide a reliable description of the magnetic field well within the Alfvén radius (Jardine et al. 2013). These plots show the largely quadrupolar field of Par 1379, and the complex field of Par 2244 that has a large fraction of energy in higher order modes.

4.3 Surface differential rotation

Our observations of Par 1379 and Par 2244 were taken over reasonably long time spans of 13 d (2.3 rotation cycles) and 26 d (9.3 rotation cycles), respectively, making them well suited to measuring differential rotation in the same way as has been carried out in several previous studies (e.g. Donati, Collier Cameron & Petit 2003; Donati et al. 2010a, 2014, 2015). We achieve this by assuming that the rotation rate at the surface of the star is varying with latitude θ as $\Omega_{\rm eq} - d\Omega \sin^2\theta$, where $\Omega_{\rm eq}$ is the rotation rate at the equator and $d\Omega$ is the difference in rotation rate between the equator and the pole. One can then reconstruct brightness and magnetic maps at a given information content for many pairs of $\Omega_{\rm eq}$ and $d\Omega$, finding the corresponding reduced chi-squared $\chi^2_{\rm r}$ at which the modelled spectra fit the observations. The topology of the resulting $\chi^2_{\rm r}$ surface usually has a well-defined minimum, and by fitting a parabola to this surface, we may estimate both $\Omega_{\rm eq}$ and $d\Omega$, and their corresponding error bars. This process has proved reliable for estimating surface differential rotation on various kinds of active low-mass stars (e.g. Donati et al. 2003, 2010a) including wTTSs (Skelly et al. 2008, 2010; Donati et al. 2014, 2015), and we refer the reader to these papers for further details of this technique.

The low $v \sin i$ of Par 1379 means our maps have a coarser spatial resolution (as compared to Par 2244), reducing the accuracy to which we can measure differential rotation. However, the large, fairly narrow plage region extending across $\sim 70^\circ$ in latitude (see Fig. 5) is well suited for measuring rotation periods and recurrence rates of profile distortions across different latitudes. Fig. 8 shows the $\chi^2_{\rm r}$ surface we obtain (as a function of $\Omega_{\rm eq}$ and $d\Omega$) for both Stokes I and V, for Par 1379. We find a clear minimum at $\Omega_{\rm eq} = 1.125 \pm 0.007$ rad d^{-1} and $d\Omega = 0.039 \pm 0.014$ for Stokes I data (corresponding to rotation periods of 5.585 ± 0.035 d at the equator and 5.786 ± 0.07 d at the poles; see the left-hand panel of Fig. 8), with the fits to the Stokes V data of $\Omega_{\rm eq} = 1.118 \pm 0.011$ rad d^{-1} and $d\Omega = 0.039 \pm 0.023$ showing consistent estimates, though with larger error bars (the right-hand panel of Fig. 8).

For Par 2244, we find a clear minimum in the χ^2 surface for Stokes I data at $\Omega_{\rm eq} = 2.2276 \pm 0.0004$ rad d^{-1} and $d\Omega = 0.0075 \pm 0.0017$ rad d^{-1} (the left-hand panel of Fig. 9). Likewise, we also find a clear minimum for the fits to Stokes V data at $\Omega_{\rm eq} = 2.218 \pm 0.0018$ rad d^{-1} and $d\Omega = 0.0306 \pm 0.0067$

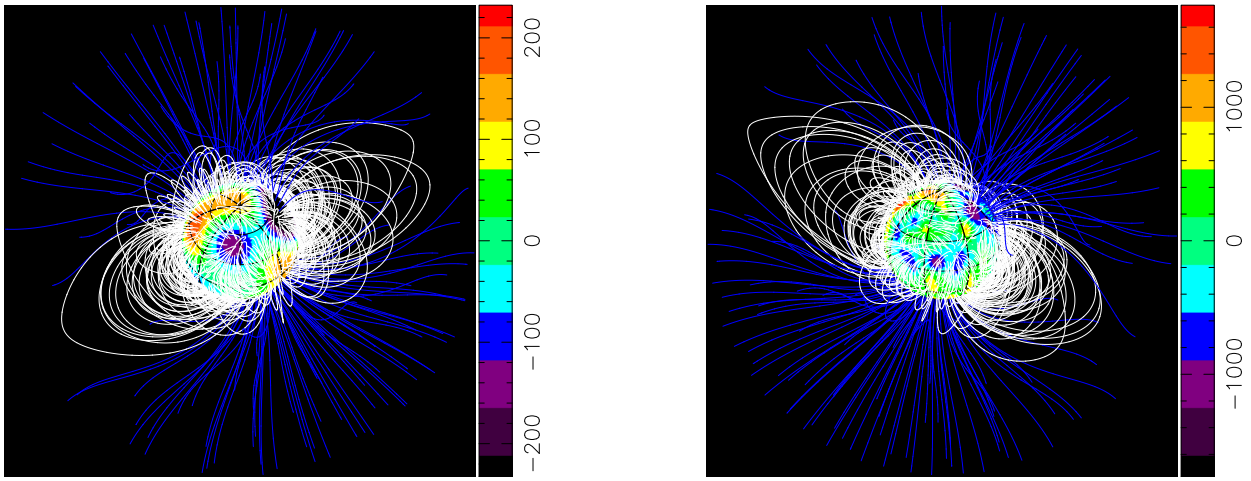

Figure 7. Potential field extrapolations of the magnetic field reconstructed for Par 1379 (left) and Par 2244 (right), viewed at inclinations of 36° and 59°, at phases 0.0 and 0.95, respectively. Open and closed field lines are shown in blue and white, respectively, whereas colours at the stellar surface depict the local values (in G) of the radial field (as shown in the left-hand panels of Fig. 6). The source surfaces at which the field becomes radial are set at distances of 5.5 $R_\star$ for Par 1379 and 2.7 $R_\star$ for Par 2244, as these are close to the co-rotation radii (where the Keplerian orbital period equals the stellar rotation period, and beyond which the field lines tend to open under the effect of centrifugal forces, Jardine 2004), but are smaller than the Alfvén radii of >10 $R_\star$ (Réville et al. 2016). This figure is best viewed in colour. Full animations may be found for both Par 1379 and Par 2244 at http://imgur.com/a/qwAXg.

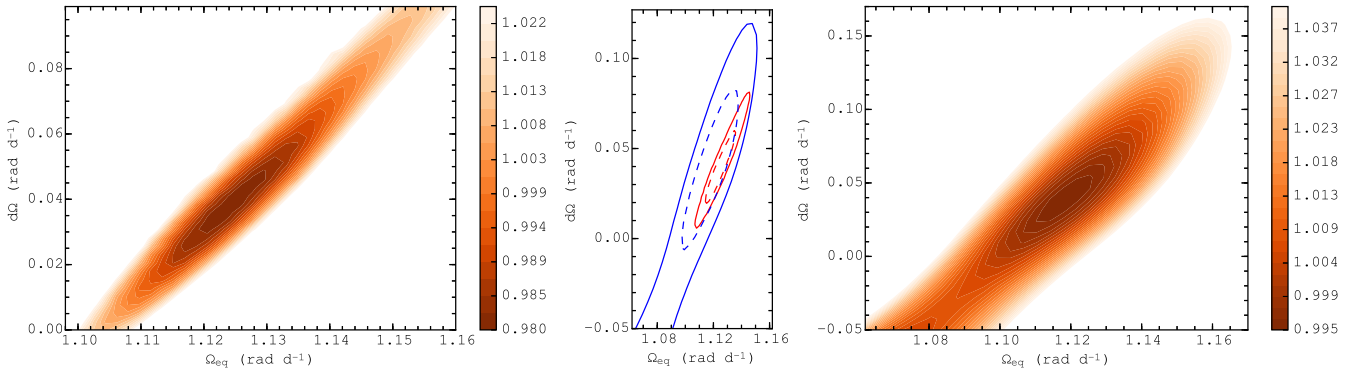

Figure 8. Variations of χ_r^2 as a function of Ω_{eq} and dΩ, derived from modelling of our Stokes *I* (left-hand panel) and Stokes *V* (right-hand panel) LSD profiles of Par 1379 at a constant information content. In both cases, a clear and well-defined parabola is observed, with the outer contour tracing the 4.5 per cent increase in χ_r^2 (or equivalently a χ^2 increase of 11.8 for 260 fitted data points) that corresponds to a 3σ ellipse for both parameters as a pair. The centre panel shows how well the confidence ellipses from both measurements overlap, with 1σ and 2σ ellipses (respectively depicting the 68.3 per cent and 95.5 per cent confidence levels) shown in solid and dashed lines (in red and blue for Stokes *I* and *V* data, respectively). This figure is best viewed in colour.

(the right-hand panel of Fig. 9). While these estimates do not agree within the formal error bars of the parabolic fit (to the region around the minimum), the minima found for each data set do however overlap at the 3σ level (see centre panel of Fig. 9). We attribute the discrepancy between minima to the temporal evolution of spots and plages over the observation window, confusing the measurements for Stokes *I* data. This line of reasoning is supported by the fact that, for the same level of information content (i.e. unsigned magnetic field strength), we cannot fit the Stokes *V* data to as low a χ^2 using the optimum Ω_{eq} and $d\Omega$ from the Stokes *I* differential rotation measurements (we find a significant increase in χ^2 of 10.7 for 1246 data points). Furthermore, we obtain better fits to the Stokes *I* data when it is split into two groups that were obtained at similar times, and fit using Ω_{eq} and $d\Omega$ derived from Stokes *V* data (further discussed in Section 5). Hence, we consider the values of Ω_{eq} and $d\Omega$ derived from Stokes *V* data to be more robust (giving rotation periods of 2.8153 ± 0.0023 d at the equator and 2.872 ± 0.039 d at the poles).

We note that the values of Ω_{eq} and $d\Omega$ determined above (for both brightness and magnetic maps, for both stars) do not change significantly when the LSD profiles are fit to different levels of information content (fitting to 30 per cent less and 5 per cent more information, compared to that for $\chi_r^2 = 1$), demonstrating the robustness of this method against under or over-fitting the data. Furthermore, the rotation periods of Par 1379 and Par 2244 determined from our analysis agree (to within 1 and 2σ) with the photometric periods found by Rebull (2001) of 5.62 ± 0.009 d and 2.82 ± 0.002 d, respectively.

5 FILTERING THE ACTIVITY JITTER TO SEARCH FOR HOT JUPITERS

As well as studying the topology of magnetic fields, the MaTYSSE programme also aims to detect potential hJs to quantitatively assess the likelihood of the disc migration scenario (where giant planets form in the outer accretion disc and then migrate inward until

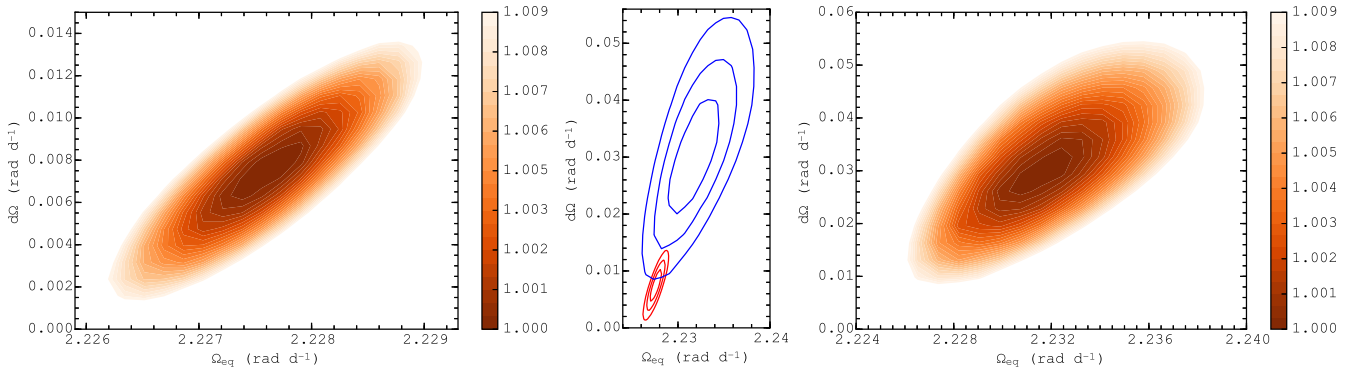

Figure 9. Same as for Fig. 8 but for Par 2244. For both Stokes *I* and *V*, a well-defined parabola is observed, with the outer contour tracing the 0.95 per cent increase in χ^2_r (or equivalently a χ^2 increase of 11.8 for 1246 fitted data points) that corresponds to a 3σ ellipse for both parameters as a pair. The centre panel shows the overlap of the confidence ellipses from both measurements, with 1σ, 2σ and 3σ ellipses shown (respectively depicting the 68.3, 95.5 and 99.7 per cent confidence levels) in red and blue for Stokes *I* and *V* data, respectively. This figure is best viewed in colour.

they reach the central magnetospheric gaps of cTTSs, see e.g. Lin, Bodenheimer & Richardson 1996; Romanova & Lovelace 2006). We achieve this in practice by filtering out the activity-related jitter from the RV curves of wTTS, by subtracting the first-order moments of our fits to the LSD profiles, from those of the observed data (following the methods outlined in Donati et al. 2014, 2015). Then, once the predicted activity jitter has been removed, one can look for periodic signals in the RV residuals that may probe the presence of hJs. This method has been used with great success for other stars in the MaTYSSE sample, leading to the detection of a hJ around both V830 Tau (Donati et al. 2015, 2016, 2017) and TAP 26 (Yu et al. 2017).

Fig. 10 shows the predicted activity jitter and filtered RVs we derive for Par 1379 and Par 2244. For Par 1379, the filtering process is very efficient, with the RV residuals exhibiting an rms dispersion of $\sim$0.017 km s^{-1}. These low residuals demonstrate that we are able to fit the simple surface features of Par 1379 to a very high degree – well below the intrinsic RV precision of ESPaDOnS (around 0.03 km s^{-1}, e.g. Moutou et al. 2007; Donati et al. 2008), and to a similar level as the intrinsic uncertainty of the filtering process itself (around 0.01 km s^{-1} in this case). Indeed, the filtered RVs are consistent with having zero amplitude (within their error bars). Hence, we find that Par 1379 is unlikely to host a hJ with an orbital period in the range of what we can detect (i.e. not too close to the stellar rotation period or its first harmonics; see Donati et al. 2014), with a 3σ error bar on the semi-amplitude of the RV residuals equal to 0.024 km s^{-1}, translating into a planet mass of $\simeq$0.56 M_{Jup} orbiting at $\simeq$0.1 au (assuming a circular orbit in the equatorial plane of the star; see Fig. 11).

For Par 2244, the filtered RVs showed a significant rms dispersion of 0.15 km s^{-1} (using the optimum Ω_{eq} and $d\Omega$ from Stokes *I* fitting; we find an rms dispersion of 0.14 km s^{-1} using the optimum fit to Stokes *V* data). Such a large dispersion is insignificant for assessing spot/plage coverage and magnetic field topology, but is very significant when searching for close-in giant planets. As mentioned previously, we attribute this large dispersion to the evolution of surface features over the observation gaps of two and three rotation cycles between data collection (around six and eight nights, respectively; see Section 2), as starspot lifetimes are expected to range from several weeks to months (e.g. Işik, Schüssler & Solanki 2007). To take account of this evolution in our map reconstruction and RV filtering procedure, we split the Stokes *I* LSD profiles into two groups of seven (with the first group spanning 2014 December 18–29 and the second group spanning 2015 January 06–13 , i.e. after the gap of three rotation cycles). Then, each set of seven LSD profiles was fit to the same level of spot and plage coverage as that found for the best fit to the complete data set. Adopting the optimum parameters for Stokes *I* data, this process yielded rms dispersions of the filtered RVs of 0.104 and 0.131 km s^{-1}, for the first and second maps, respectively. However, when using the optimum parameters for Stokes *V* data, we find smaller rms dispersions of 0.084 and 0.087 km s^{-1} for each map (an average of 0.086 km s^{-1}), respectively, suggesting that the differential rotation measurement from fitting Stokes *V* data is more robust against the intrinsic evolution of surface features. Indeed, the magnitude of these dispersions are similar to the 0.087 km s^{-1} uncertainties on the filtered RVs, showing that our tomographic modelling can account for the majority of the RV variability. These residuals are lower than our detection threshold of $\simeq$0.1 km s^{-1} (from preliminary simulations, see Donati et al. 2014). Furthermore, we find no significant peaks in a Lomb–Scargle periodogram of the filtered RVs. Thus, we conclude that Par 2244 is unlikely to host a hJ with an orbital period of what we can detect, with a 3σ error bar on the semi-amplitude of the RV residuals equal to 0.206 km s^{-1}, translating into a value of $\sim$3.54 M_{Jup} for a planet orbiting at a distance of 0.1 au (again assuming a circular orbit in the equatorial plane of the star; see Fig. 11).

We note that we also fit both Stokes *I* and Stokes *V* profiles simultaneously for each group of 7 profiles, with the resulting magnetic field topologies being largely similar to that found when fitting all 14 profiles, except that the unsigned field strength was around 20 per cent lower. However, we were unable to reliably constrain a measurement of differential rotation using only seven profiles.

6 DISCUSSION

We have reported results from our spectropolarimetric observations collected with ESPaDOnS of the wTTSs Par 1379 and Par 2244, in the framework of the international MaTYSSE Large Programme.

We find that both stars have largely similar atmospheric properties, with photospheric temperatures of 4600 ± 50 and 4650 ± 50 K, and logarithmic gravities in cgs units of 3.9 ± 0.2 and 4.1 ± 0.2. These properties suggest that Par 1379 and Par 2244 are of a similar mass (1.6 ± 0.1 and 1.8 ± 0.1 $M_\odot$), with respective radii of 2.7 ± 0.2 and 3.5 ± 0.2 $R_\odot$, viewed at inclinations of 36° and 59°.

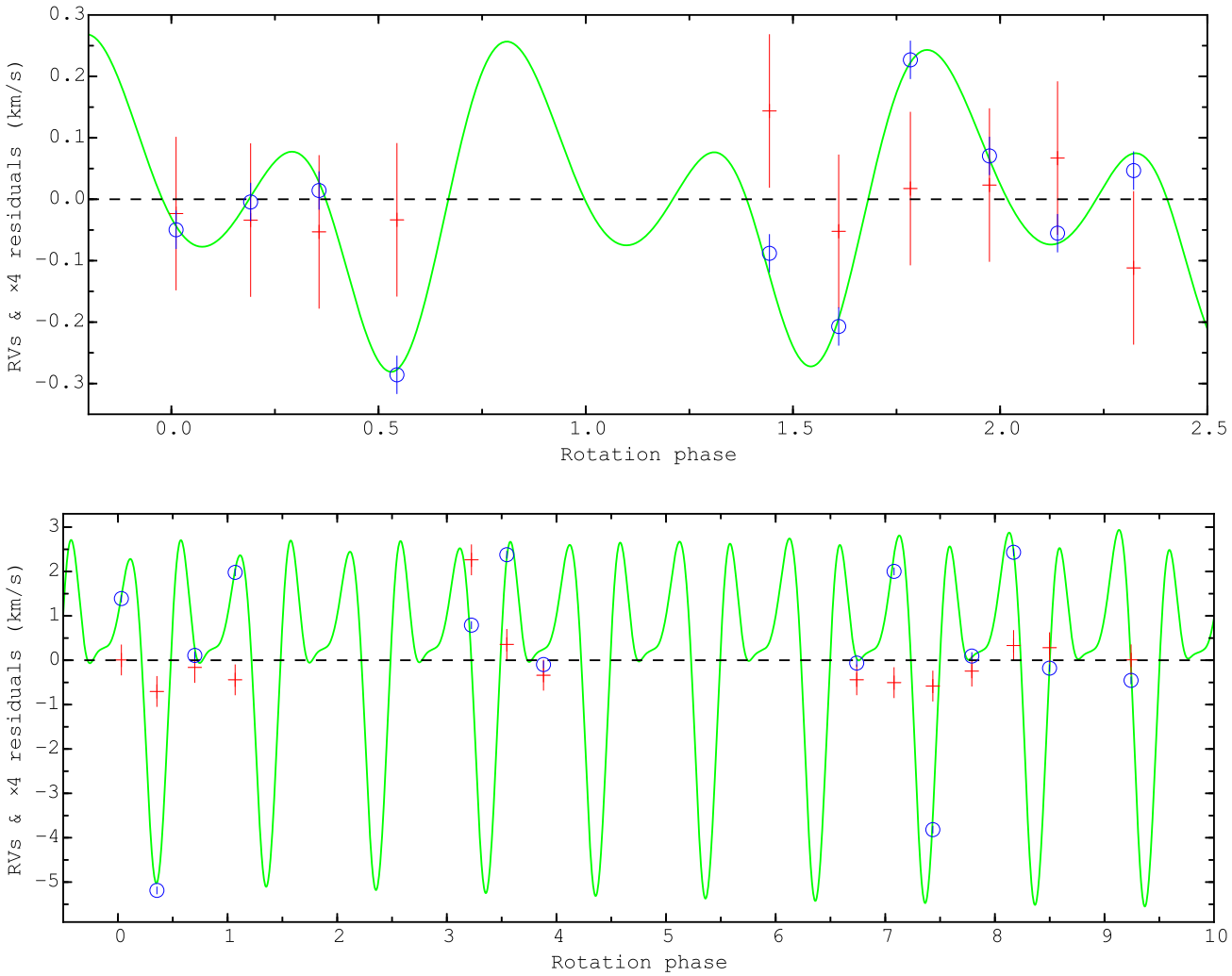

Figure 10. RV variations (in the stellar rest frame) of Par 1379 (top) and Par 2244 (bottom) as a function of rotation phase, as measured from our observations (open blue circles) and predicted by the tomographic brightness maps of Fig. 5 (green line). RV residuals are also shown (red crosses, with values and error bars scaled by a factor of 4 for clarity), and exhibit a rms dispersion equal to 0.017 km s^{-1} for Par 1379 and 0.086 km s^{-1} for Par 2244. Note that the RV residuals for Par 2244 are those measured from the two separate maps. RVs are estimated as the first-order moment of the Stokes *I* LSD profiles rather than through Gaussian fits, due to their asymmetric and often irregular shape. This figure is best viewed in colour.

We estimate their ages to be Myr, with internal structures that are both around 70 per cent convective by radius (using Siess et al. 2000 evolutionary models).

The stars' rotation periods of 5.585 and 2.8153 d for Par 1379 and Par 2244, respectively, are similar to those of the (lower mass) wTTSs, V819 Tau and V830 Tau Donati et al. (2015), but are much slower than V410 Tau (a wTTSs with similar mass and position in the H–R diagram, rotating in 1.87 d). Furthermore, our targets' periods lie within the uniform period distribution between 1 and 8 d of the vast majority of stars in the ONC flanking fields Rebull (2001).

We find that Par 1379 harbours a dusty circumstellar disc with an inner radius of around 0.15 au, and with a dust mass ranging between 10^{-7} and 10^{-5} M$_\odot$, with Par 2244 surrounded by a either primordial dust, or a debris disc (starting around 20 au). This may explain why Par 1379 rotates slower than Par 2244, despite being a similar age, suggesting that Par 2244 has dissipated its (presumably less massive) accretion disc somewhat sooner than Par 1379 and has spent more time spinning up.

By using common tracers of accretion (see Section 3.3), we find that Par 1379 and Par 2244 may be accreting at levels of $\log \dot{M}_{\rm acc} \simeq -10$ to -11 M$_\odot$ yr^{-1}. Given that this accretion rate is so low, our measurements are likely to be strongly affected by chromospheric emission, and so they must be taken as upper limits. These very low accretion rates suggest that these targets may be classed as wTTSs.

As the accretion rates for Par 1379 are low, there may be other explanations for the absorption features seen in Hα that are unrelated to inflow along an accretion funnel. Using our map of surface magnetic fields (see Section 4.2), we have compared the observed variations in Hα in Fig. A1 with our potential field extrapolation (see Fig. A2). At cycle 0.191, we see the (observed) maximum of redshifted absorption in Hα, with the potential field extrapolation showing several large active regions, with many closed magnetic loops, some of which are aligned along the line of sight. At cycle 0.544, we see no redshifted absorption in Hα, with few regions of closed loops in the field extrapolation, but rather mainly open field lines. Finally, cycle 1.783 also shows no redshifted absorption, but

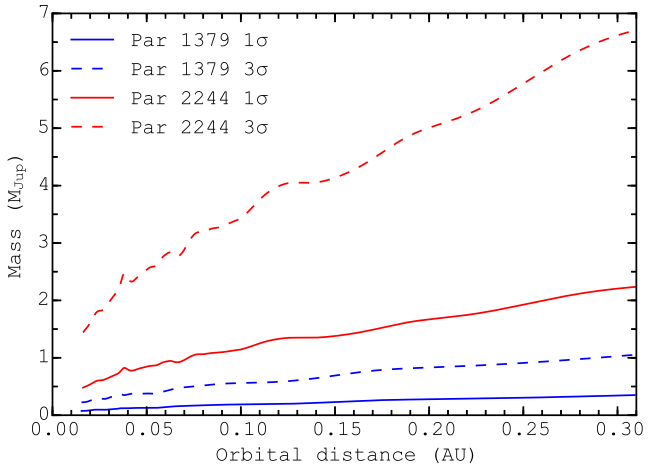

Figure 11. The 1σ and 3σ upper limits (solid and dashed lines, respectively) on the recovered planet mass as a function of orbital distance, using the RVs shown in Fig. 10 for Par 1379 (blue) and Par 2244 (red). This figure is best viewed in colour.

rather blueshifted emission, with the extrapolation showing a region of many closed loops, aligned with the line of sight.

Given that the absorption appears when we see closed magnetic loops, it may be caused by an infall of material along these loops from flare or prominence material (as seen in the late-type rapid-rotator LO Peg, see Eibe et al. 1999). Furthermore, the strongest absorption occurs around $140\,\mathrm{km\,s^{-1}}$ – the same as the free-fall velocity of the star, and so infalling material from the top of the larger loops could create such absorption features. Moreover, the blueshifted emission (seen prominently at cycle 1.783) may trace the same prominence material that falls down towards the star in front of the disc around phase 0.2; the material may have be seen off the stellar limb (as a result of the low inclination), and is thus in emission and moving towards the observer (while still falling on to the star) around half a rotation cycle later. Alternatively, the blueshifted emission may be caused by erupting prominence material along sight-aligned loops.

If the redshifted absorption were due to inflow along an accretion funnel, we would expect to see maximum absorption when many open field lines (that are able to connect to the inner disc) are aligned along the line of sight. This is not the case, as there is no absorption at, for example, cycle 0.544 (see Fig. A2), where many open field lines are seen. Additionally, we note that while Megeath et al. (2012) place Par 1379 near the limit between wTTSs and cTTSs, Rebull (2001) report a very regular periodic light curve for Par 1379 that does not appear like that of a cTTS, with Rebull et al. (2000) reporting a lack of UV excess, further supporting the non-accreting hypothesis.

Using our tomographic imaging code (adapted for wTTSs, see Donati et al. 2014), we derived surface brightness maps and magnetic topologies of both stars. Cool spots and warm plages are found on both Par 1379 and Par 2244, with the latter exhibiting more complex features with higher contrast, that appear to show some intrinsic evolution over our $\sim$1 month observing window.

The reconstructed magnetic fields for Par 1379 and Par 2244 are significantly different in both strength and topology. Par 1379 harbours a predominately non-axisymmetric poloidal field (3/4 of the total field), with the largest fraction of energy in the quadrupolar mode, and where the large-scale magnetosphere of the poloidal field is inclined at $\simeq 65^\circ$ to the rotation axis. In contrast, the field of Par 2244 is split 3:2 into a mostly non-axisymmetric poloidal component (with half of the reconstructed energy in modes with $\ell \geq 4$), tilted at $\simeq 45^\circ$ from the rotation axis, and a mostly axisymmetric toroidal component.

The magnetic field of Par 2244 is fairly similar in strength and topology to that of V410 Tau, the wTTS lying closest in the H–R diagram that has been mapped with ZDI ($M_\star = 1.4 \pm 0.2$ M$_\odot$, age $\simeq$1.2 Myr, average unsigned field strength 0.49 kG; Skelly et al. 2010). The fields of both of these stars are split fairly evenly between a mostly non-axisymmetric poloidal component, and a toroidal component, with a similarly high number of modes required to fit the data ($\ell \leq 18$ for Par 2244, $\ell = 15$ for V410 Tau).

Compared to the lower mass wTTSs, V819 Tau and V830 Tau, Par 2244 has a similar field strength, but is much more complex (Donati et al. 2015). The field strength of Par 1379 is also weaker than that of Tap 35 (1500 G), but is similar to the 700 G field of Tap 10 (Basri, Marcy & Valenti 1992). In contrast, the much less complex field of Par 1379 is also much weaker than any other wTTSs that has been mapped to date, suggesting it is likely to be more structurally evolved than Par 2244 [assuming the magnetic topology is related to the development of a radiative core, based on Siess et al. (2000) models], becoming largely radiative already, despite model predictions.

A comprehensive analysis of the similarity between magnetic fields of wTTSs and cTTSs is still premature at this stage. For completeness, however, we show in Fig. 12 an H–R diagram of the cTTSs from the MaPP programme, as well as the (analysed) MaTYSSE wTTSs. Fig. 12 also indicates the fraction of the field that is poloidal, the axisymmetry of the poloidal component, and shows PMS evolutionary tracks from Siess et al. (2000). One can see that the wTTSs studied thus far generally show a wider range of field topologies compared to cTTSs, with large-scale fields that can be more toroidal and non-axisymmetric (also see discussion in Donati et al. 2015). Clearly, given our limited sample of wTTSs with which to compare field strength and topology, further studies of MaTYSSE stars are required before we can carry out a full analysis.

Our data indicate that significant latitudinal shear has occurred for both brightness and magnetic maps over the observation timescales for each star (14 and 25 nights, respectively). For Par 1379, we estimated the amount of differential rotation to be non-zero at a confidence level of 99.5 per cent, with a shear rate 1.4× smaller than that of the Sun (with an equator-pole lap time of $\simeq$160 d, as opposed to $\simeq$110 d for the Sun). Furthermore, the estimates derived from brightness and magnetic maps agree to within their error bars. For Par 2244, we estimate the amount of differential rotation to be non-zero at a confidence level of over 99.99 per cent (for both brightness and magnetic maps). We find that the intrinsic evolution of surface features over our observation window resulted in a much lower shear rate for the brightness maps, as compared to the magnetic maps (with shear rates 7.3× and 1.8× smaller than the Sun, for Stokes I and Stokes V data, respectively). However, by accounting for this evolution, we show that the estimate from the magnetic maps is more robust, and so determine the equator-pole lap time to be $\simeq$205 d. Our results show higher shear rates than those for other wTTSs that have had a similar measurement, namely TWA 6, V410 Tau, V819 Tau, V830 Tau, LkCa 4 and TAP 26 (Skelly et al. 2008, 2010; Donati et al. 2014, 2015; Yu et al. 2017). However, all these stars (apart from V410 Tau) have significantly different masses, and occupy a different part of the H–R diagram. Furthermore, our measured shear rates are similar to that found for a cTTS with similar properties, namely V2129 Oph (where the shear is 1.5× smaller than the Sun, Donati et al. 2011).

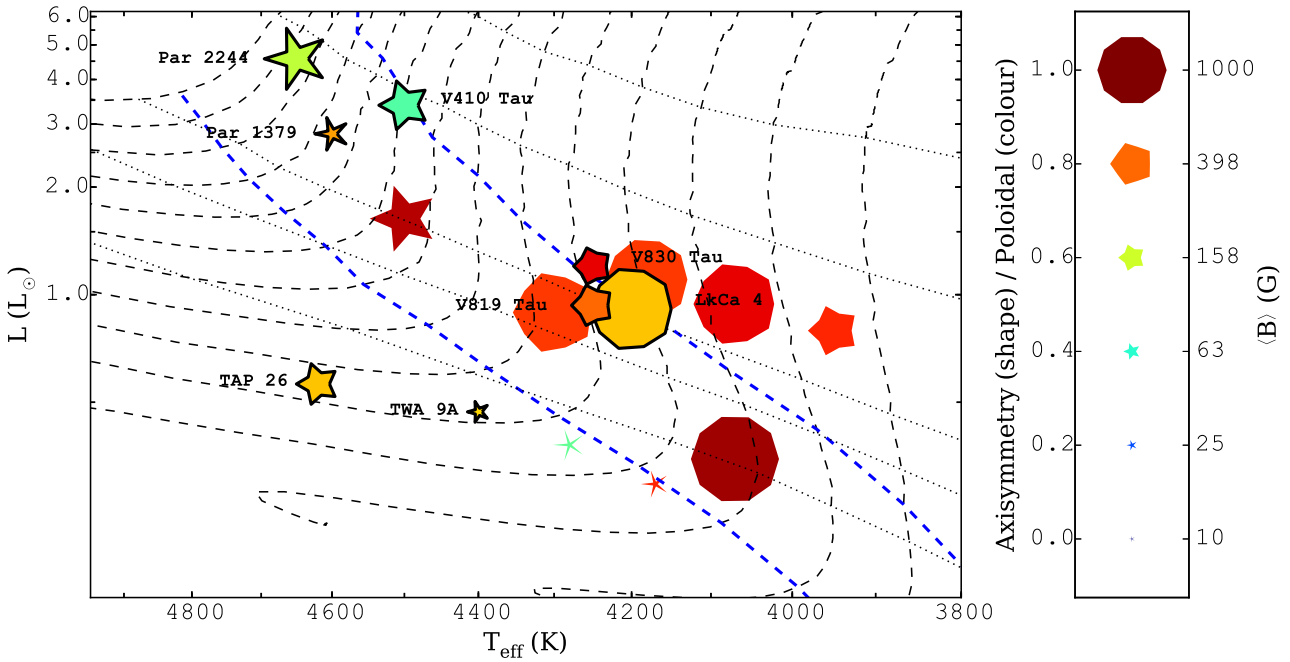

Figure 12. H–R diagram showing the MaTYSSE wTTSs (black line border and labelled) and the MaPP cTTSs (no border). The size of the symbols represents the surface-averaged magnetic field strength (with a larger symbol meaning a stronger field), the colour of the symbol represents the fraction of the field that is poloidal (with red being completely poloidal), and the shape of the symbols represents the axisymmetry of the poloidal field component (with higher axisymmetry shown as a more circular symbol). Also shown are evolutionary tracks from Siess et al. (2000) (black dashed lines, ranging from 0.5 to 1.9 $M_{\odot}$), with corresponding isochrones (black dotted lines, for ages of 0.5, 1, 3, 5 and 10 Myr), and lines showing 100 per cent and 50 per cent convective interior by radius (blue dashed).

Using our tomographic maps to predict the activity-related RV jitter, we were able to filter the RV curves of both stars in the search for potential hJs (in the same manner as Donati et al. 2014, 2015). For Par 1379, we find that the activity jitter is filtered down to an rms RV precision of 0.017 km s^{-1}, a value similar to the intrinsic uncertainty of the filtering process itself, and lower than the RV stability of ESPaDOnS. With no significant peaks in a Lomb–Scargle periodogram of the filtered RVs, we find that Par 1379 is unlikely to host a hJ with an orbital period of what we can detect, with a 3σ error bar on the semi-amplitude of the RV residuals equal to 0.024 km s^{-1}, translating into a planet mass of $\simeq$0.56 M_{Jup} orbiting at $\simeq$0.1 au. For Par 2244, we find a significantly larger rms dispersion of 0.086 km s^{-1} ; however, these residuals are lower than our estimated detection threshold for hJs ($\simeq$0.1 km s^{-1}, see Donati et al. 2014). Furthermore, we find no significant peaks in a Lomb–Scargle periodogram of the filtered RVs, and thus conclude that Par 2244 is unlikely to host a hJ with an orbital period of what we can detect, with a 3σ error bar on the semi-amplitude of the RV residuals equal to 0.206 km s^{-1}, translating into a value of $\sim$3.54 M_{Jup} for a planet orbiting at a distance of 0.1 au.

7 SUMMARY

We report the results of our spectropolarimetric monitoring of the wTTSs Par 1379 and Par 2244, within the MaTYSSEprogramme. We have determined out target stars to be of a similar mass (1.6 and 1.8 $M_{\odot}$) and age (1.8 and 1.1 Myr), with Par 1379 hosting an evolved low-mass dusty circumstellar disc, and with Par 2244 showing evidence of a young debris disc. Using several accretion diagnostics, we find that the stars may be accreting at a very low level; however, our derived accretion rates are strongly influenced by chromospheric emission (due to stellar activity), and so are likely unreliable. Using tomographic imaging, we have modelled the rotational modulation of line profile distortions and Zeeman signatures, yielding brightness and magnetic maps of the surface. We find that Par 1379 harbours a weak (250 G), mostly poloidal field tilted 65° from the rotation axis. In contrast, Par 2244 hosts a stronger field (860 G) split 3:2 between poloidal and toroidal components, with most of the energy in higher order modes, and with the poloidal component tilted 45° from the rotation axis. Compared to the lower mass wTTSs, V819 Tau and V830 Tau, Par 2244 has a similar field strength, but is much more complex, whereas the much less complex field of Par 1379 is also much weaker than any other mapped wTTS. We find moderate surface differential rotation of 1.4× and 1.8× smaller than Solar. Using our tomographic maps to predict the activity-related RV jitter, and filter it from the RV curves, we find RV residuals with dispersions of 0.017 and 0.086 km s^{-1} for Par 1379 and Par 2244, respectively. We find no evidence for close-in giant planets around either star, with 3σ upper limits of 0.56 and 3.54 M_{Jup} (at an orbital distance of 0.1 au).

ACKNOWLEDGEMENTS

This paper is based on observations obtained at the CFHT, operated by the National Research Council of Canada, the Institut National des Sciences de l'Univers of the Centre National de la Recherche Scientifique (INSU/CNRS) of France and the University of Hawaii. We thank the CFHT QSO team for its great work and effort at collecting the high-quality MaTYSSE data presented in this paper. MaTYSSE is an international collaborative research programme involving experts from more than 10 different countries (France, Canada, Brazil, Taiwan, UK, Russia, Chile, USA, Switzerland, Portugal, China and Italy). We also warmly thank the IDEX initiative at Université Fédérale Toulouse Midi-Pyrénées (UFTMiP) for

funding the STEPS collaboration programme between IRAP/OMP and ESO and for allocating a 'Chaire d'Attractivité' to GAJH, allowing her to regularly visit Toulouse to work on MaTYSSE data. SGG acknowledges support from the Science & Technology Facilities Council (STFC) via an Ernest Rutherford Fellowship [ST/J003255/1]. SHPA acknowledges financial support from CNPq, CAPES and Fapemig. This work has made use of the VALD, operated at Uppsala University, the Institute of Astronomy RAS in Moscow, and the University of Vienna, and the SVO Filter Profile Service supported from the Spanish MINECO through grant AyA2014-55216. We thank Christophe Pinte for the use of his MCFOST radiative transfer code, and Belinda Nicholson for providing the data point for TWA 9A in Fig. 12.

REFERENCES

Aarnio A. N., Matt S. P., Stassun K. G., 2012, ApJ, 760, 9
Alcalá J. M. et al., 2017, A&A, 600, A20
Alibert Y., Mordasini C., Benz W., Winisdoerffer C., 2005, A&A, 434, 343
André P., Basu S., Inutsuka S., 2009, The Formation and Evolution of Prestellar Cores. Cambridge Univ. Press, Cambridge, p. 254
Andrews S. M., Williams J. P., 2005, ApJ, 631, 1134
Baraffe I., Homeier D., Allard F., Chabrier G., 2015, A&A, 577, A42
Barrado y Navascués D., Martín E. L., 2003, AJ, 126, 2997
Baruteau C. et al., 2014, in Beuther H., Klessen R. S., Dullemond C. P., Henning T., eds, Protostars and Planets VI. University of Arizona Press, Tucson, p. 667
Basri G., Marcy G. W., Valenti J. A., 1992, ApJ, 390, 622
Bessell M. S., Brett J. M., 1988, PASP, 100, 1134
Bouvier J., Alencar S. H. P., Harries T. J., Johns-Krull C. M., Romanova M. M., 2007, in Reipurth B., Jewitt D., Keil K., eds, Protostars and Planets V. University of Arizona Press, Tucson, p. 479
Carpenter J. M., Hillenbrand L. A., Skrutskie M. F., 2001, AJ, 121, 3160
Carroll T. A., Strassmeier K. G., Rice J. B., Künstler A., 2012, A&A, 548, A95
Chabrier G., Baraffe I., 1997, A&A, 327, 1039
Cranmer S. R., 2009, ApJ, 706, 824
Cranmer S. R., Saar S. H., 2011, ApJ, 741, 54
Davies C. L., Gregory S. G., Greaves J. S., 2014, MNRAS, 444, 1157
Donati J. F. et al., 2016, Nature, 534, 662
Donati J.-F., 2001, in Boffin H. M. J., Steeghs D., Cuypers J., eds, Lecture Notes in Physics, Vol. 573, Astrotomography, Indirect Imaging Methods in Observational Astronomy. Springer Verlag, Berlin, p. 207
Donati J.-F., 2003, in Trujillo-Bueno J., Sanchez Almeida J., eds, ASP Conf. Ser. Vol. 307, Solar Polarization. Astron. Soc. Pac., San Francisco, p. 41
Donati J.-F., Landstreet J. D., 2009, ARA&A, 47, 333
Donati J.-F., Semel M., Carter B. D., Rees D. E., Collier Cameron A., 1997, MNRAS, 291, 658
Donati J.-F., Collier Cameron A., Petit P., 2003, MNRAS, 345, 1187
Donati J.-F. et al., 2006, MNRAS, 370, 629
Donati J.-F. et al., 2007, MNRAS, 380, 1297
Donati J.-F. et al., 2008, MNRAS, 385, 1179
Donati J.-F. et al., 2010a, MNRAS, 402, 1426
Donati J.-F. et al., 2010b, MNRAS, 409, 1347
Donati J.-F. et al., 2011, MNRAS, 412, 2454
Donati J.-F. et al., 2012, MNRAS, 425, 2948
Donati J.-F. et al., 2013, MNRAS, 436, 881
Donati J.-F. et al., 2014, MNRAS, 444, 3220
Donati J.-F. et al., 2015, MNRAS, 453, 3706
Donati J.-F. et al., 2017, MNRAS, 465, 3343
Draine B. T., Lee H. M., 1984, ApJ, 285, 89
Durney B. R., De Young D. S., Roxburgh I. W., 1993, Sol. Phys., 145, 207
Eibe M. T., Byrne P. B., Jeffries R. D., Gunn A. G., 1999, A&A, 341, 527
Fang M., van Boekel R., Wang W., Carmona A., Sicilia-Aguilar A., Henning T., 2009, A&A, 504, 461
Frank A. et al., 2014. Protostars and Planets VI, Beuther H., Klessen R. S., Dullemond C. P., Henning T., eds, Univ. Arizona Press, Tucson, p. 451
Fűrész G., Hartmann L. W., Megeath S. T., Szentgyorgyi A. H., Hamden E. T., 2008, ApJ, 676, 1109
Gaia Collaboration et al., 2016, A&A, 595, A2
Gilliland R. L., 1986, ApJ, 300, 339
Gregory S. G., Donati J.-F., Morin J., Hussain G. A. J., Mayne N. J., Hillenbrand L. A., Jardine M., 2012, ApJ, 755, 97
Gull S., Skilling J., 1991, Quantified Maximum Entropy MemSys5 User's Manual. Maximum Entropy Data Consultants. Available at: https://books.google.co.uk/books?id=_sFHHQAACAAJ
Gullbring E., Hartmann L., Briceño C., Calvet N., 1998, ApJ, 492, 323
Gully-Santiago M. A. et al., 2017, ApJ, 836, 200
Hussain G. A. J. et al., 2009, MNRAS, 398, 189
Ingleby L. et al., 2011, ApJ, 743, 105
Işik E., Schüssler M., Solanki S. K., 2007, A&A, 464, 1049
Jardine M., 2004, A&A, 414, L5
Jardine M., Collier Cameron A., Donati J.-F., 2002, MNRAS, 333, 339
Jardine M., Vidotto A. A., van Ballegooijen A., Donati J.-F., Morin J., Fares R., Gombosi T. I., 2013, MNRAS, 431, 528
Johns-Krull C. M., Valenti J. A., Koresko C., 1999, ApJ, 516, 900
Kounkel M. et al., 2017, ApJ, 834, 142
Kurucz R. L., 1993, CDROM Model Distribution, Smithsonian Astrophys. Obs.
Landi Degl'Innocenti E., Landolfi M., 2004, Polarization in Spectral Lines. No. 307 in Astrophysics and Space Library. Kluwer Academic Publishers, Dordrecht/Boston/London
Landin N. R., Mendes L. T. S., Vaz L. P. R., Alencar S. H. P., 2016, A&A, 586, A96
Lin D. N. C., Bodenheimer P., Richardson D. C., 1996, Nature, 380, 606
Manara C. F. et al., 2013, A&A, 551, A107
Matt S. P., Pinzón G., Greene T. P., Pudritz R. E., 2012, ApJ, 745, 101
Megeath S. T. et al., 2012, AJ, 144, 192
Morin J. et al., 2008, MNRAS, 390, 567
Moutou C. et al., 2007, A&A, 473, 651
Natta A., Testi L., Muzerolle J., Randich S., Comerón F., Persi P., 2004, A&A, 424, 603
Newton E. R., Irwin J., Charbonneau D., Berlind P., Calkins M. L., Mink J., 2017, ApJ, 834, 85
Pecaut M. J., Mamajek E. E., 2013, ApJS, 208, 9
Pinte C., Ménard F., Duchêne G., Bastien P., 2006, A&A, 459, 797
Pinte C., Harries T. J., Min M., Watson A. M., Dullemond C. P., Woitke P., Ménard F., Durán-Rojas M. C., 2009, A&A, 498, 967
Rebull L. M., 2001, AJ, 121, 1676
Rebull L. M., Hillenbrand L. A., Strom S. E., Duncan D. K., Patten B. M., Pavlovsky C. M., Makidon R., Adams M. T., 2000, AJ, 119, 3026
Reggiani M., Robberto M., Da Rio N., Meyer M. R., Soderblom D. R., Ricci L., 2011, A&A, 534, A83
Reiners A., Schüssler M., Passegger V. M., 2014, ApJ, 794, 144
Réville V., Folsom C. P., Strugarek A., Brun A. S., 2016, ApJ, 832, 145
Romanova M. M., Lovelace R. V. E., 2006, ApJ, 645, L73
Ryabchikova T., Piskunov N., Kurucz R. L., Stempels H. C., Heiter U., Pakhomov Y., Barklem P. S., 2015, Phys. Scr, 90, 054005
Siess L., Dufour E., Forestini M., 2000, A&A, 358, 593
Skelly M. B., Unruh Y. C., Collier Cameron A., Barnes J. R., Donati J.-F., Lawson W. A., Carter B. D., 2008, MNRAS, 385, 708
Skelly M. B., Donati J.-F., Bouvier J., Grankin K. N., Unruh Y. C., Artemenko S. A., Petrov P., 2010, MNRAS, 403, 159
Tobin J. J., Hartmann L., Furesz G., Mateo M., Megeath S. T., 2009, ApJ, 697, 1103
Valenti J. A., Fischer D. A., 2005, ApJS, 159, 141
Vidotto A. A. et al., 2014, MNRAS, 441, 2361
Werner M. W. et al., 2004, ApJS, 154, 1
White R. J., Basri G., 2003, ApJ, 582, 1109
Wright E. L. et al., 2010, AJ, 140, 1868
Yu L. et al., 2017, MNRAS, 467, 1342
Zacharias N. et al., 2015, AJ, 150, 101

APPENDIX A: PAR 1379 H α AND H β LINE PROFILES, AND POTENTIAL FIELD EXTRAPOLATIONS, PAR 2244 H α LINE PROFILES

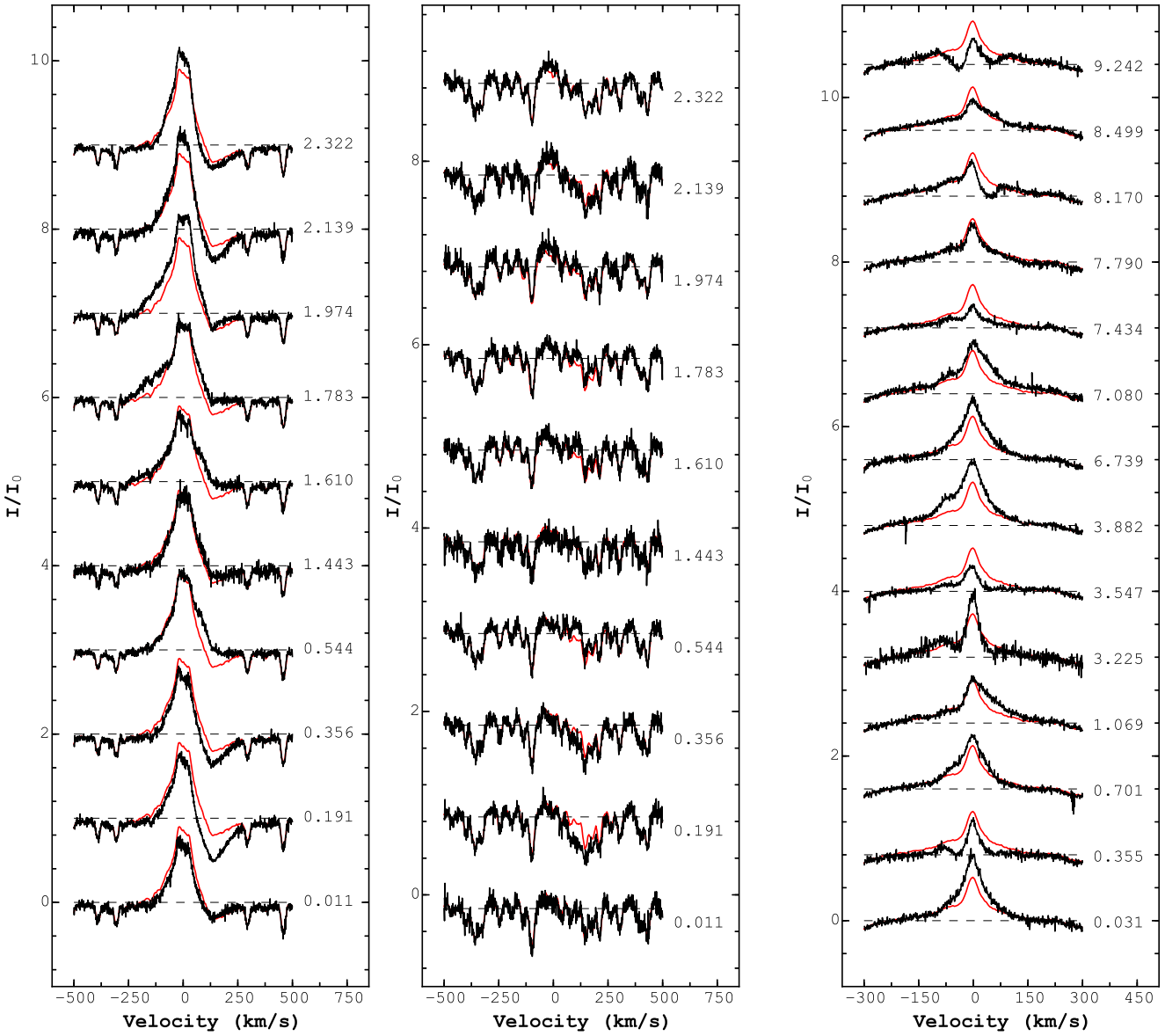

Figure A1. H α and H β line profiles for Par 1379 (left, centre) and H α line profiles for Par 2244 (right), all shown as black solid lines, where the mean line profile is shown in red, and the continuum as a black dashed line, with the cycle number displayed on the right of each profile.

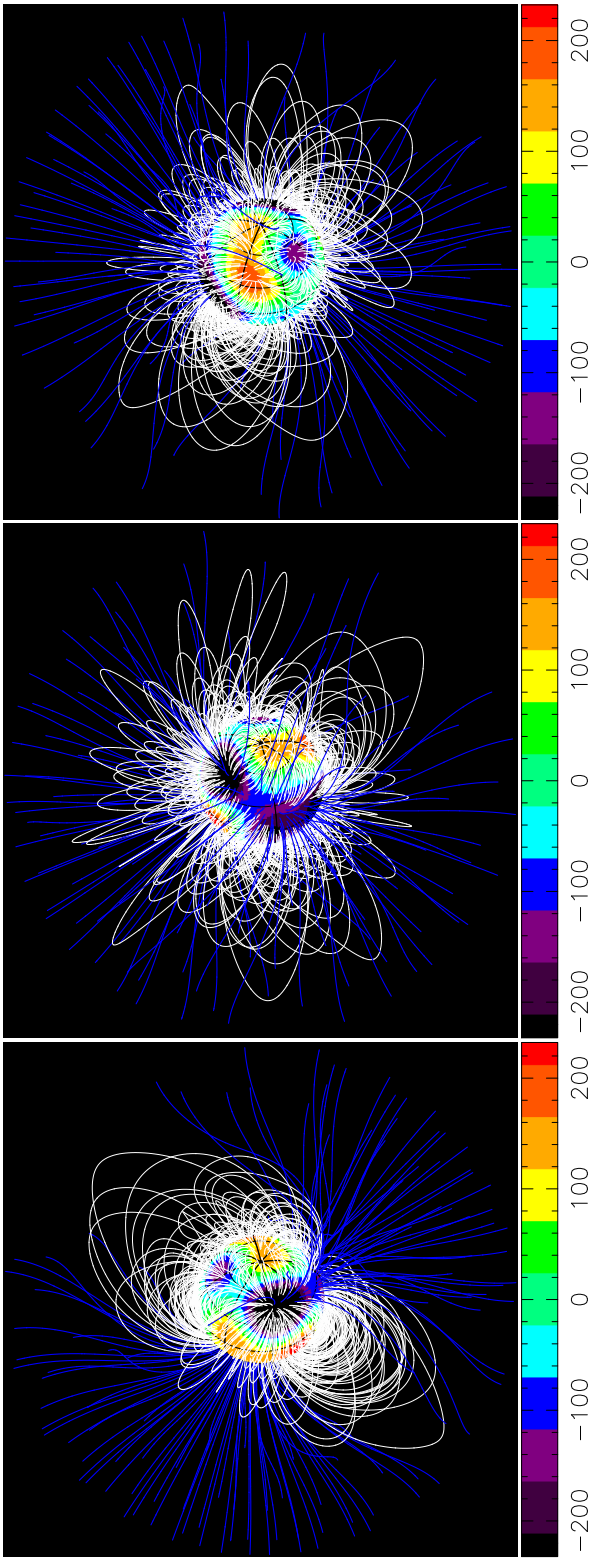

Figure A2. Potential extrapolations of the magnetic field reconstructed for Par 1379 (as for Fig. 7), shown at phases 0.191 (top), 0.544 (middle) and 1.783 (bottom). A full animation may be found online at http://imgur.com/a/qwAXg.

APPENDIX B: SED-FITTING PROBABILITY AND HISTOGRAM PLOTS

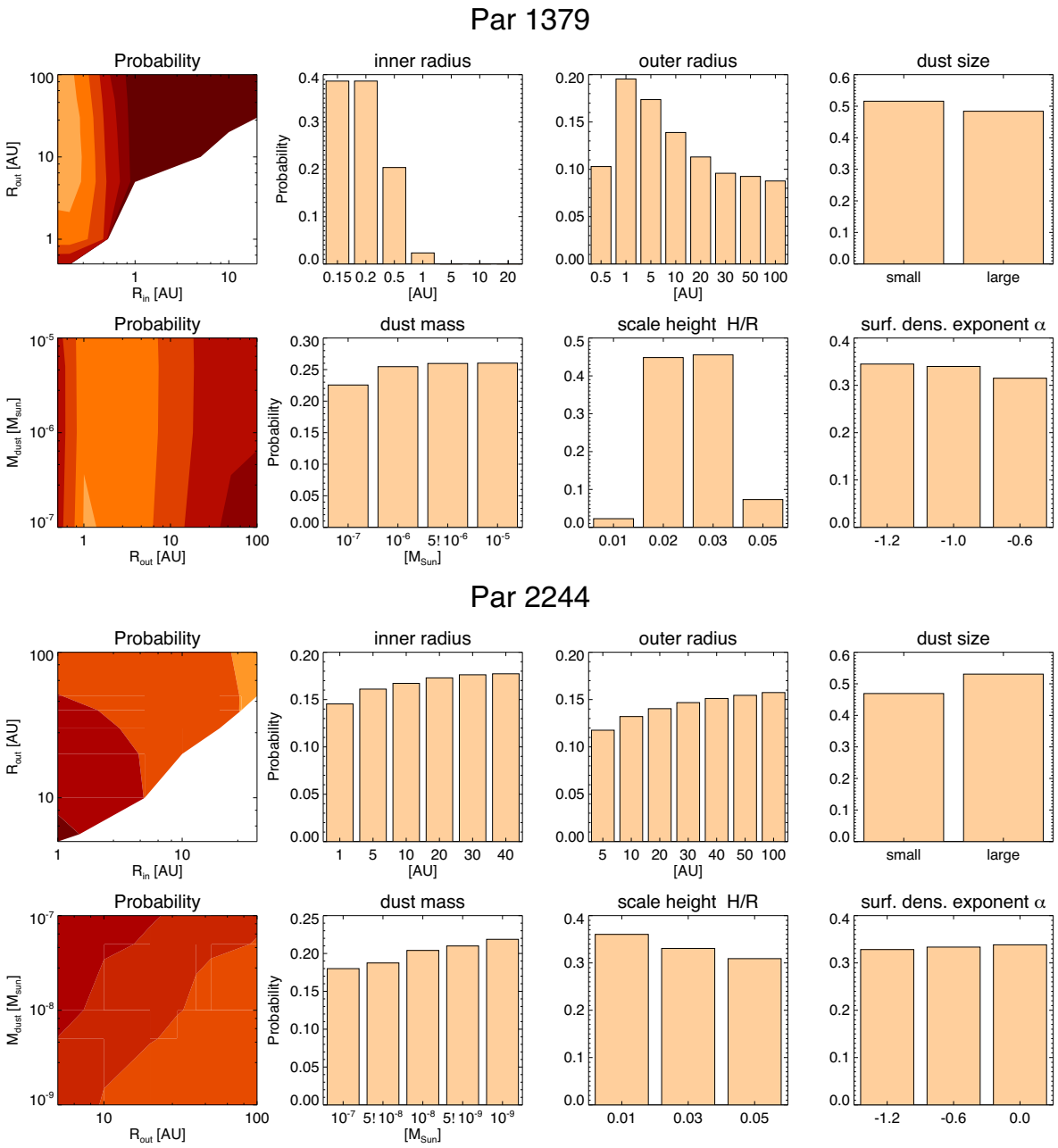

Figure B1. 2D probability and histograms of the grid of SED models calculated for Par 1379 and Par 2244. The colour code in the $R_{\rm out}$ versus $R_{\rm in}$ and $M_{\rm dust}$ versus $R_{\rm out}$ contour plots is $P = 0.01$, 0.02, 0.03, 0.04 and 0.05, from dark red to orange, with lighter colours being a higher probability.

This paper has been typeset from a TEX/LATEX file prepared by the author.